
Where Pretraining writes and Alignment reads: the asymmetry of Transformer weight space

Valeria Ruscio, Eli-Shaoul Khedouri, Keiran Thompson
Intuition Machines
valeria.ruscio@intuitionmachines.com

Abstract

Cross-entropy pretraining and preference alignment update the same transformer weights, but leave geometrically distinct traces. We characterise this asymmetry with a relative-subspace-fraction probe that tracks how weight deltas align with residual-stream activation subspaces and with the prediction subspace defined by the unembedding. Alignment deltas concentrate in the read pathway (W_Q, W_K), along principal directions of attention-input activations, while remaining near-isotropic in the write pathway (W_O, W_2) relative to the prediction subspace. We explain this pattern through anisotropic gradient accumulation: updates to a matrix W are sums of outer products $\delta_t a_t^\top$, and inherit directional structure from whichever side has concentrated covariance. For read-pathway matrices, this side is the input activation a_t , whose covariance is spiked in trained transformers and therefore produces objective-agnostic concentration. For write-pathway matrices, the relevant side is the upstream gradient δ_t , whose anisotropy depends on the loss. Cross-entropy supplies the canonical sharp per-sample signal, inducing write-pathway prediction geometry during pretraining; alignment objectives typically add little further write-side concentration. We support this explanation with a within-checkpoint trajectory, a graded contrastive-objective control, and a closed-form rank-1 intervention with matched direction controls, providing causal evidence for the proposed weight-space geometry.

1 Introduction

Modern language models are typically trained in stages. Cross-entropy pretraining installs broad predictive competence, and preference alignment then shifts the model’s behaviour using supervised or preference-based objectives. These phases are often analysed separately, but they act on the same transformer weights. This raises a structural question: when alignment modifies a pretrained model, where in weight space does its effect accumulate, and why does it accumulate there? We answer this question with a geometric probe of weight deltas. The resulting pattern is asymmetric. Alignment deltas show elevated read-pathway RSF (W_Q, W_K) in the principal subspace of attention-input activations relative to an isotropic null. A finer per-direction diagnostic shows that this elevation is not covariance-proportional: alignment deltas are anti-aligned with the top activation PCs relative to their eigenvalue mass, with above-null RSF surviving because activation covariance is highly spiked. By contrast, they remain near-isotropic in the *write pathway* (W_O, W_2) with respect to the prediction manifold spanned by the top singular vectors of the unembedding W_U . This read/write dissociation appears across six base architectures and three model families, and is robust to the choice of projector source, calibration distribution, and alignment stage.

We explain the asymmetry through anisotropic gradient accumulation. A weight update is a sum of rank-one outer products, $\delta_t a_t^\top$, so the accumulated delta inherits directional structure from whichever side of the outer product has spectrally concentrated covariance. The relevant side differs between pathways. For matrices that read from the residual stream, the input-side activations a_t determine the

row-space structure; because activation covariance is spiked in trained transformers, read-pathway deltas concentrate under many objectives. For matrices that write into the residual stream, the relevant structure comes from the upstream gradient δ_t , whose anisotropy depends on the loss.

Cross-entropy pretraining is the canonical sharp-gradient regime: one-hot targets produce concentrated per-sample gradients, which install prediction-aligned structure in W_O and W_2 during pretraining. Other objectives produce this structure only to the extent that their per-sample signals are sharp: contrastive losses with hard negatives do so partially, whereas diffuse-negative objectives do not. Preference alignment therefore adds little further prediction-aligned structure to the write pathway, which has already been organised by pretraining. Its dominant geometric trace instead appears in the read pathway, where spiked activation covariance continues to shape deltas across objectives.

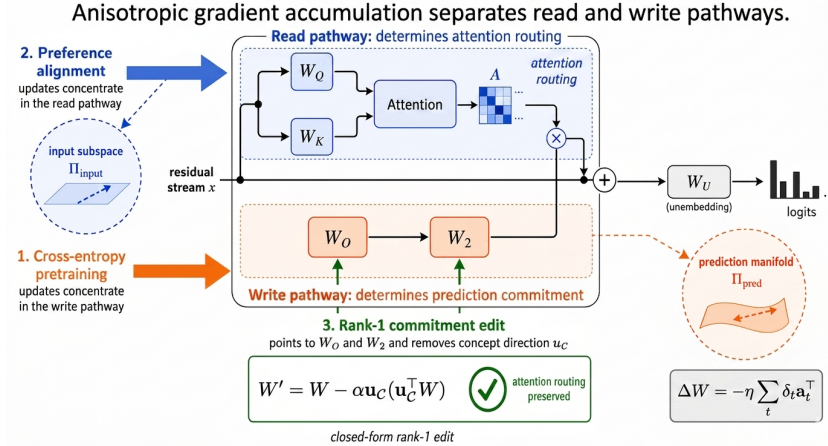


Figure 1: Anisotropic gradient accumulation separates transformer read and write pathways. Read-pathway updates inherit structure from spiked residual-stream activations. Write-pathway updates inherit structure from upstream gradients; cross-entropy pretraining induces prediction-aligned geometry in Π_{pred} , the top singular subspace of W_U . The rank-1 edit tests this write-pathway geometry along a concept direction u_c .

2 Related Work

Elhage et al. [2021] formalise the residual stream as a shared communication channel between attention and MLP sublayers; our write/read partition refines this decomposition by identifying which matrices write structured information into the residual stream and which read from it. Geva et al. [2022, 2021] show that MLP layers act as key-value memories whose values are interpretable in vocabulary space; our framework provides a geometric account of why this vocabulary alignment arises and predicts its restriction to the write pathway. The logit lens [nostalgebraist, 2020] and tuned lens [Belrose et al., 2023a] project intermediate hidden states through W_U ; our prediction manifold Π_{pred} is the subspace in which these projections are informative.

ROME [Meng et al., 2022a] and MEMIT [Meng et al., 2022b] introduce rank-1 edits on MLP W_2 to modify factual associations, located via causal tracing and computed by an optimisation step against a target key-value pair. Our rank-1 edit shares only the algebraic form: its target is not a localised factual association but a column-space orientation predicted by the framework geometry, computed in closed form from W_U rows with no causal-tracing or optimisation step. The two methods address different problems, ROME locates and modifies a specific fact; our edit reverses a geometric commitment direction the theory identifies, and we use it as a falsifiable test of the theory rather than as an editing method. LEACE [Belrose et al., 2023b] and concept-erasure work [Ravfogel et al., 2022] operate in activation space; representation engineering [Zou et al., 2023] intervenes at inference time. Our intervention operates in weight space on the write pathway, which preserves alignment routing (concentrated in the read pathway) by construction.

Spectral structure of transformer weights has been studied for training dynamics [Martin and Mahoney, 2021], compression [Sharma et al., 2023], and emergent low-rank structure [Hsu et al., 2022, Jaiswal

et al., 2023]. The RSF probe differs in measuring the relative orientation of weight changes against a reference subspace, enabling cross-pathway and cross-phase comparison. Task arithmetic [Ilharco et al., 2023] and model merging [Yadav et al., 2023, Wortsman et al., 2022] compose fine-tuning deltas additively; our finding that alignment and pretraining induce orthogonal structures in distinct matrices provides a geometric account of why such composition often preserves each contribution. Work on preference learning geometry [Rafailov et al., 2023, Hong et al., 2024] treats DPO and ORPO as distribution-alignment objectives; we provide a complementary weight-space characterisation locating where these objectives deposit their induced deltas. Recent work on inference-time logit optimisation [Wang et al., 2026] establishes a sample-space dual to KL-regularised RL training; our weight-space characterisation of where DPO deposits its delta provides a natural empirical complement to that perspective. Our findings are a weight-space companion to feature-level linguistic neural collapse [Wu and Pappan, 2024a]. Where Wu and Pappan [2024a] describe the collapse of features around within-class means in the final hidden state, we identify the weight matrices in which the supporting structure accumulates and the conditions under which it does. The two probes co-occur in models where late layers commit strongly to next-token prediction and diverge in models where late layers preserve contextual structure. This is consistent with both phenomena being downstream manifestations of the same representation-subspace formation process during training.

3 Methodology

A transformer decoder layer updates a residual stream $\mathbf{h}^{(\ell)} \in \mathbb{R}^d$ through attention and MLP sublayers. We partition the layer’s weight matrices by how they interact with this stream. The *write pathway* ($W_O \in \mathbb{R}^{d \times d_v}$, $W_2 \in \mathbb{R}^{d \times d_{tr}}$) writes into the residual stream, while the *read pathway* ($W_Q \in \mathbb{R}^{d_k \times d}$, $W_K \in \mathbb{R}^{d_k \times d}$) reads from it. Thus write-pathway columns and read-pathway rows both lie in \mathbb{R}^d , but play opposite functional roles. The unembedding $W_U \in \mathbb{R}^{V \times d}$ maps the final residual stream to logits and defines the prediction-aligned subspace used below.

This partition is functional rather than notational. Section 4 shows that read- and write-pathway matrices are governed by different sources of gradient anisotropy. The remaining matrices, W_V in attention and W_1 in the MLP, are internal to their sublayers: they couple to the residual stream only through downstream matrices (W_O and W_2). The chain rule therefore predicts that they inherit read-pathway geometry in attenuated form. Appendix C.4 confirms this and extends the two-pathway partition to a three-tier hierarchy. Appendix B describes other experimental setup details.

3.1 Geometric probes

Relative subspace fraction Let $\mathbf{\Pi} \in \mathbb{R}^{d \times d}$ be an orthogonal projector onto a k -dimensional residual-stream subspace. For a weight matrix or weight delta \mathbf{W} , we define

$$\text{RSF}(\mathbf{W}, \mathbf{\Pi}) = \frac{\text{tr}(\mathbf{W}^\top \mathbf{\Pi}_L \mathbf{W}) + \text{tr}(\mathbf{W} \mathbf{\Pi}_R \mathbf{W}^\top)}{\|\mathbf{W}\|_F^2}, \quad (1)$$

where $\mathbf{\Pi}_L = \mathbf{\Pi}$ and $\mathbf{\Pi}_R = \mathbf{0}$ for write-pathway matrices, and $\mathbf{\Pi}_L = \mathbf{0}$ and $\mathbf{\Pi}_R = \mathbf{\Pi}$ for read-pathway matrices. The projector is therefore always applied on the residual-stream side of the matrix: columns for matrices that write to the residual stream, and rows for matrices that read from it. In both cases $\text{RSF} \in [0, 1]$, with null value k/d for a rotationally uniform matrix.

We use two RSF protocols. In the *static delta protocol*, $\mathbf{W} = \Delta W = W_{\text{aligned}} - W_{\text{base}}$ for an alignment-stage checkpoint paired with its base model. The normalized quantity $\text{RSF}(\Delta W, \mathbf{\Pi})/(k/d)$ measures how strongly the alignment delta is oriented toward a reference subspace. This is the protocol used for the cross-family alignment-delta experiments.

In the *within-checkpoint protocol*, $\mathbf{W} = W^{(t)}$ is the full weight matrix at pretraining step t , and $\mathbf{\Pi}^{(t)}$ is recomputed from the same checkpoint. This measures how the current weights align with the current geometry, rather than with a base-to-aligned delta. We use this protocol for the Pythia trajectory analysis in Section 5.2.

Projectors We construct three rank- k projectors, with $k = 50$ in the main experiments. $\mathbf{\Pi}_{\text{pred}}$ is the span of the top- k right singular vectors of the unembedding W_U . We call this the *prediction manifold*, since it is the subspace through which unembedding-projected gradients $W_U^\top(\mathbf{p} - \mathbf{e}_{y^*})$ enter the final-layer write pathway. $\mathbf{\Pi}_{\text{input}}$ is obtained by PCA of residual-stream activations at each

layer, and captures the principal input subspace for read-pathway matrices. $\mathbf{\Pi}_{\text{behav}}$ is obtained by PCA of final-layer activation differences $\mathbf{h}_{\text{aligned}} - \mathbf{h}_{\text{base}}$, and captures the dominant behavioural displacement induced by alignment¹.

Principal-subspace overlap For two k -dimensional subspaces of \mathbb{R}^d with orthonormal bases $V_1, V_2 \in \mathbb{R}^{d \times k}$, we measure overlap by the mean squared principal-angle cosine

$$\text{overlap}(V_1, V_2) = \frac{1}{k} \|V_1^\top V_2\|_F^2 = \frac{1}{k} \sum_{i=1}^k \sigma_i^2(V_1^\top V_2). \quad (2)$$

This quantity equals 1 when the subspaces coincide and 0 when they are orthogonal. If one k -dimensional subspace is chosen uniformly at random independently of the other, its expectation is k/d .

3.2 Operational Test of Pathway Symmetry

The static RSF protocol measures the geometric structure of accumulated deltas. To test whether write- and read-pathway perturbations propagate through the residual stream symmetrically once injected, we apply a layer-local perturbation probe at a chosen layer $\ell^* = \lfloor 2L/3 \rfloor$. Two interventions of equal Frobenius magnitude with identical target direction \mathbf{u}_C are applied:

$$W_O \leftarrow W_O - \alpha \mathbf{u}_C (\mathbf{u}_C^\top W_O), \quad W_2 \leftarrow W_2 - \alpha \mathbf{u}_C (\mathbf{u}_C^\top W_2), \quad (3)$$

$$W_Q \leftarrow W_Q - \alpha (W_Q \mathbf{u}_C) \mathbf{u}_C^\top, \quad W_K \leftarrow W_K - \alpha (W_K \mathbf{u}_C) \mathbf{u}_C^\top. \quad (4)$$

We then measure the resulting change in attention logits at every layer ℓ :

$$M_1(\ell) = \|QK_{\text{edit}}^\top(\ell) - QK_{\text{base}}^\top(\ell)\|_F. \quad (5)$$

Two predictions follow from forward-pass order alone, independent of the framework. At ℓ^* the write-side edit is invisible to attention because W_O, W_2 act on the residual stream after attention has been computed; the read-side edit perturbs QK^\top directly. The empirical content lies at $\ell > \ell^*$: if the residual stream acts as a source-agnostic communication channel, perturbations of equal magnitude should propagate downstream comparably regardless of pathway of origin. We report $M_1^{\text{read}}(\ell)/M_1^{\text{write}}(\ell)$ averaged over the ten layers following ℓ^* . Concept direction \mathbf{u}_C is matched to the rank-1 suppression target of Section 5.4 and intervention strength $\alpha = 0.5$.

3.3 Causal Probe: Rank-1 Commitment Edit

The framework yields a closed-form intervention. The **rank-1 edit**

$$W_2^{(\ell)} \leftarrow W_2^{(\ell)} - \alpha \hat{\mathbf{u}}_y (\hat{\mathbf{u}}_y^\top W_2^{(\ell)}), \quad \hat{\mathbf{u}}_y = W_U[y] / \|W_U[y]\| \quad (6)$$

reverses the column-space component of $W_2^{(\ell)}$ pointing toward a target unembedding direction. At $\alpha = 1$ the edit is a rank-1 projection onto the null space of $\hat{\mathbf{u}}_y$; at intermediate α it attenuates without fully removing. The identical edit applies to $W_O^{(\ell)}$.

For *concept-level* suppression, the single-token direction is replaced by a normalised weighted centroid of multiple token unembedding directions:

$$\mathbf{u}_C = \frac{\sum_i w_i \hat{\mathbf{u}}_i}{\|\sum_i w_i \hat{\mathbf{u}}_i\|}. \quad (7)$$

When concept tokens have high pairwise cosine similarity the centroid captures most surface-form variants simultaneously. Section 5.4 uses the intervention as a falsifiable test of the framework’s directional commitments, with random-direction and bottom-spectrum-direction controls at matched Frobenius magnitude (Appendix K).

¹For matrices with more than 4000 rows, we use sliced truncated SVD. Results are stable for $k \in [32, 64]$ (Appendix C.1). By default, $\mathbf{\Pi}_{\text{input}}$ is computed from base-model activations on WikiText-2. Appendix C.2 repeats the analysis on C4, OASST1, and Alpaca; Appendix C.3 shows that recomputing the projector from aligned-model activations changes the read-pathway RSF ratio by less than 0.07.

4 Anisotropic Gradient Accumulation

We explain the write/read dissociation through a simple property of gradient accumulation. For any linear map W , the per-sample gradient has outer-product form,

$$\nabla_W \mathcal{L} = \sum_t \delta_t \mathbf{a}_t^\top, \quad \Delta W = -\eta \sum_{t=1}^T \delta_t \mathbf{a}_t^\top, \quad (8)$$

where \mathbf{a}_t is the activation feeding W and δ_t is the upstream gradient. The accumulated delta can inherit directional structure from either side of this outer product: row-space structure from the activations $\{\mathbf{a}_t\}$, and column-space structure from the gradients $\{\delta_t\}$. Which side matters depends on the matrix’s role in the residual stream.

The key asymmetry is that the relevant source of anisotropy is objective-agnostic for read-pathway matrices but loss-dependent for write-pathway matrices. Read-pathway matrices receive the residual stream as input, and residual-stream activations in trained transformers have spiked covariance. Write-pathway matrices receive upstream gradients shaped by the training objective, so their concentration depends on whether the loss produces sharp per-sample gradient structure.

4.1 Two Pathways, Two Conditions

Read pathway: input-side anisotropy For $W_Q^{(\ell)}$ and $W_K^{(\ell)}$, the input side of the gradient outer product is the residual-stream activation, $\mathbf{a}_t = \mathbf{h}_t^{(\ell)}$. Therefore $\Delta W_Q^{(\ell)}$ and $\Delta W_K^{(\ell)}$ have row-space structure determined by the span and covariance of $\{\mathbf{h}_t^{(\ell)}\}_t$. Since trained transformers typically have spiked residual-stream covariance, the principal activation subspace provides a stable target for read-pathway concentration.

This condition is largely objective-agnostic: any objective that updates attention weights uses the same activation-side geometry. The magnitude of concentration can vary across objectives, because the upstream gradients $\delta_{Q,t}^{(\ell)}$ change with the loss and data, but the reference subspace is set by the activation distribution.

Write pathway: gradient-side anisotropy For $W_O^{(\ell)}$ and $W_2^{(\ell)}$, the residual-stream-aligned side is the output side of the matrix. At the final layer under cross-entropy loss,

$$\delta^{(L)} = W_U^\top (\mathbf{p} - \mathbf{e}_{y^*}), \quad (9)$$

so the upstream gradient lies in $\text{row}(W_U)$. However, membership in $\text{row}(W_U)$ does not by itself imply concentration in the top singular subspace of W_U . Concentration requires the empirical distribution of upstream gradients to be anisotropic within that row space.

This condition is loss-specific. Objectives with sharp per-sample signals produce structured upstream gradients and can concentrate write-pathway weights in prediction-aligned directions. Objectives with diffuse per-sample signals need not do so. The gradient accumulation therefore predicts a read-side elevation that is stable in subspace across objectives, and a write-side response whose magnitude is graded by per-sample gradient sharpness.

4.2 The Cross-Entropy Case

Cross-entropy pretraining is the canonical sharp-gradient regime. For target token y^* and output distribution $\mathbf{p} \in \Delta^{V-1}$, the logit gradient is

$$\nabla_{\mathbf{z}} \mathcal{L} = \mathbf{p} - \mathbf{e}_{y^*}. \quad (10)$$

For a fixed target, the negative gradient points toward the simplex vertex \mathbf{e}_{y^*} : probability mass is removed from non-target tokens and added to the target token. Across training examples, this creates sharp per-sample gradient directions tied to individual vocabulary vertices. After multiplication by W_U^\top , these vertex-directed signals become upstream gradients in the prediction geometry of the residual stream. We use *simplex-vertex attractor* to refer to this mechanism: cross-entropy repeatedly pulls each example toward a one-hot target, producing concentrated upstream-gradient structure. Other objectives can produce weaker versions of this condition. Contrastive losses with hard negatives, for example, supply a distinguished positive target against a small set of strong alternatives; diffuse-negative losses spread gradient mass more broadly. The write-pathway prediction is therefore graded rather than binary (Section 5.3).

4.3 Containment and Concentration

The gradient-accumulation separates two claims.

Containment: Some subspace constraints follow directly from the chain rule. At the final layer, any logit-routed loss satisfies

$$\nabla_{\mathbf{h}^{(L)}} \mathcal{L} = W_U^\top \nabla_{\mathbf{z}} \mathcal{L} \in \text{row}(W_U),$$

so the column space of $\Delta W_2^{(L)}$ and $\Delta W_O^{(L)}$ is contained in $\text{row}(W_U)$. Similarly, read-pathway gradients have row space contained in the span of the residual-stream inputs, because each update is proportional to $\delta_t \mathbf{h}_t^{(\ell)\top}$.

Concentration: Containment only identifies the ambient subspace. It does not say where mass lies inside that subspace. Concentration depends on empirical spectral structure: for the read pathway, the principal subspace of activation covariance Σ_h ; for the write pathway, the spectral concentration of the upstream-gradient distribution $\{\delta_t\}_t$. These quantities are measurable, but their magnitudes are not derived from first principles here. The framework predicts the qualitative pattern: objective-stable read-pathway concentration and loss-dependent write-pathway concentration.

4.4 Pretraining induces the Geometry

The two conditions predict a specific static signature for alignment deltas. During cross-entropy pretraining, sharp per-sample gradients install prediction-aligned structure in the write pathway (W_O, W_2). By the time preference alignment begins, this write-side geometry is already present. Alignment objectives that do not add similarly sharp upstream-gradient structure therefore produce near-null static deltas in the write pathway with respect to $\mathbf{\Pi}_{\text{pred}}$.

The read pathway behaves differently. Because activation covariance remains spiked during alignment, alignment deltas in W_Q and W_K continue to inherit the principal activation subspace. Thus the dominant static signature of alignment is predicted to appear in the read pathway, while the write pathway records the earlier effect of pretraining.

The within-checkpoint prediction is dynamic. During pretraining, $\text{RSF}(W_2^{(t)}, \mathbf{\Pi}_{\text{pred}}^{(t)})$ should rise as prediction-aligned residual-stream geometry forms, peak when that geometry stabilizes, and then decay toward an above-null asymptote as later updates add mass outside the leading prediction subspace. This rise–peak–decay trajectory distinguishes AGA from a monotone-growth account of write-pathway concentration.

4.5 Closed-Form Intervention

The same geometry suggests a direct intervention on the write pathway. For a target token y , define the normalized unembedding direction $\hat{\mathbf{u}}_y = W_U[y] / \|W_U[y]\|$. We edit

$$W_2^{(\ell)} \leftarrow W_2^{(\ell)} - \alpha \hat{\mathbf{u}}_y (\hat{\mathbf{u}}_y^\top W_2^{(\ell)}), \quad (11)$$

with the analogous edit applied to $W_O^{(\ell)}$. The edit removes, or for $\alpha < 1$ attenuates, the component of the write-pathway matrix pointing in the target unembedding direction.

For concept-level suppression, we replace the single-token direction with a weighted centroid of normalized unembedding directions,

$$\mathbf{u}_c = \frac{\sum_i w_i \hat{\mathbf{u}}_i}{\|\sum_i w_i \hat{\mathbf{u}}_i\|}. \quad (12)$$

If write-pathway prediction geometry is functionally involved in target-token commitment, this edit should reduce target probabilities more than matched random or bottom-spectrum directions. The intervention therefore provides a falsification test of the proposed geometry. The same account predicts a boundary condition: when alignment broadly reorganizes W_U , the centroid derived from unembedding rows can decouple from the model’s active suppression direction, and edit strength should decrease with the stable rank of ΔW_U .

5 Empirical Results

Table 30 reports the main static-delta result. Alignment deltas show a pathway-specific orientation: read-pathway matrices (W_Q, W_K) have elevated RSF in $\mathbf{\Pi}_{\text{input}}$, while write-pathway matrices

Table 1: RSF ratios relative to the k/d null. Mean \pm std across alignment-stage checkpoints. Residual-stream reads show elevated RSF in Π_{input} ; residual-stream writes sit near null on the static delta; internal-sublayer matrices inherit attenuated read geometry.

Matrix tier	Π_{pred}	Π_{input}	Π_{behav}
Residual-stream writes (W_O, W_2)	1.08 ± 0.05	1.25 ± 0.10	1.09 ± 0.05
Direct reads (W_Q, W_K)	1.10 ± 0.12	2.05 ± 0.63	1.11 ± 0.13
Internal reads (W_V, W_1)	1.05 ± 0.07	1.35 ± 0.28	—
Null	1.00	1.00	1.00

(W_O, W_2) remain near the k/d null in Π_{pred} . Cross-projector measurements cluster close to null, indicating that the effect is specific to the predicted pathway–subspace pairing rather than a generic increase in low-dimensional structure.

A mixed-effects analysis controlling for base-architecture clustering (Table 3) supports the same dissociation. The read-pathway diagonal contrast is large and significant; the write-pathway contrast is not elevated in the predicted static-delta direction. An architecture-level paired Wilcoxon test gives the same qualitative conclusion without distributional assumptions. Thus the static alignment delta is primarily a read-pathway phenomenon. The read-pathway elevation should be interpreted relative to the isotropic null, not as covariance-proportional alignment to the top activation PCs. Appendix H.1.1 measures the per-direction allocation $\hat{c}_i = (\|\Delta W_{q_i}\|^2 / \|\Delta W\|_F^2) / (\lambda_i / \text{tr}\Sigma_h)$. At $\ell^* = \lfloor 2L/3 \rfloor$, $\hat{c}_{\text{top}k}$ ranges from 0.053 to 0.156, indicating anti-alignment with the highest-variance activation directions. Nevertheless, RSF remains above k/d because activation covariance is highly spiked: the top- k directions account for $\rho_R = 0.43\text{--}0.61$ of activation trace.

The write-pathway near-null result is predicted by Section 4.4: cross-entropy pretraining has already installed prediction-aligned structure in W_O and W_2 , so alignment objectives without comparably sharp per-sample gradients add little further Π_{pred} -aligned mass. We test the write-pathway claim directly below using within-checkpoint pretraining trajectories and objective controls.

The dissociation is robust to projector construction. Recomputing Π_{input} from aligned-model rather than base-model activations changes the read-pathway ratio by less than 0.07 (mean principal-angle cosine 0.89; Appendix C.3). Repeating the analysis across calibration sources preserves the asymmetry, with larger magnitudes when the calibration distribution is closer to the alignment data (Appendix C.2).

5.1 Operational Pathway Symmetry

The RSF probe measures where accumulated deltas are geometrically oriented; it does not by itself test whether read- and write-pathway perturbations propagate differently once they enter the residual stream. We therefore apply the layer-local perturbation test from Section 3.2. At the edit layer ℓ^* , the write edit produces zero change in QK^\top by construction, because W_O and W_2 act after attention is computed, while the read edit directly perturbs attention logits. The empirical question is what happens downstream. Across the model sample, downstream propagation is nearly symmetric: the ratio $M_1^{\text{read}}/M_1^{\text{write}}$, averaged over the ten layers following ℓ^* , lies in the range 0.93–0.97 (Appendix O). Thus, once a perturbation has been injected into the residual stream, later layers propagate it similarly regardless of whether it originated in a read- or write-pathway edit. The static RSF dissociation should therefore be interpreted as a difference in where training deposits structure, not as a downstream propagation asymmetry of the residual stream.

5.2 Pretraining Installs the Write-Pathway Geometry

Table 4 reports the within-checkpoint trajectory on the Pythia suite. Write-pathway concentration in Π_{pred} follows a rise–peak–decay pattern: it is near null at step 16, peaks at step 1000, and decays to an above-null value by the final checkpoint. The peak coincides with rapid reorganization of the prediction subspace: the principal-subspace overlap $\text{overlap}(\Pi_{\text{pred}}^{(0)}, \Pi_{\text{pred}}^{(t)})$ drops from 1.00 at step 16 to near the random-subspace baseline k/d by step 1000, and remains stable thereafter. This pattern supports the pretraining account in Section 4.4. Early training forms the prediction-aligned geometry; once that geometry stabilizes, later updates add mass outside the leading prediction subspace, producing the observed decay toward an above-null asymptote. The result is difficult to reconcile with a monotone-growth account of write-pathway concentration. The trajectory is

Table 2: Rank-1 edit on natural Wikipedia continuations, $\alpha = 0.5$. $\Delta \log p_{\text{tgt}}$: target log-probability change in nats. $\Delta \log p_{\text{nbr}}$: held-out continuation change. PPL_{off} : perplexity ratio on off-concept text.

Model	Stage	$p_{\text{base}} \rightarrow p_{\text{edit}}$	$\Delta \log p_{\text{tgt}}$	$\Delta \log p_{\text{nbr}}$	PPL_{off}
Llama-3.2-3B	base	0.51 \rightarrow 0.06	-3.01	-1.70	1.05
	aligned	0.56 \rightarrow 0.13	-2.13	-0.98	1.05
Llama-3-8B	base	0.57 \rightarrow 0.04	-3.43	-1.10	1.01
	aligned	0.67 \rightarrow 0.17	-2.67	-0.30	1.01
Tulu-8B	SFT	0.62 \rightarrow 0.12	-2.65	-0.61	1.01
	DPO	0.71 \rightarrow 0.25	-1.94	-0.04	1.00
Qwen-2.5-3B	aligned	0.42 \rightarrow 0.14	-2.29	-1.23	1.08
Qwen-2.5-7B	aligned	0.40 \rightarrow 0.07	-2.81	-0.67	1.11
Mistral-7B	aligned	0.73 \rightarrow 0.48	-0.92	+0.20	1.00

single-family, since Pythia is the available public suite with suitable intermediate checkpoints, but the final above-null signature is consistent with the cross-model static evidence in Table 30.

5.3 Graded Objective-Dependence

The gradient accumulation predicts different objective-dependence in the two pathways: read-pathway concentration should persist across objectives because it is driven by activation-side anisotropy, whereas write-pathway concentration should scale with the sharpness of the per-sample upstream gradient. Table 5 tests this prediction using contrastive fine-tuning pairs. The write-pathway result is graded. Encoder InfoNCE pairs and GTE-Qwen2 sit near the Π_{pred} null, while E5-Mistral retains partial write-pathway concentration. This ordering matches the expected sharpness of the training signal: diffuse in-batch negatives produce weak per-sample commitment, while hard-negative retrieval training supplies a more concentrated signal. The result argues against a chain-rule-only explanation, under which any logit-routed objective should produce comparable write-pathway concentration. The read-pathway result persists across all contrastive fine-tunes. A matched-architecture comparison on Mistral-7B (Mistral-Instruct vs. E5-Mistral) controls for architecture and scale: both objectives produce above-null read-pathway concentration, with larger magnitude under SFT (paired Wilcoxon $p < 10^{-3}$; Appendix I). Thus the read-pathway subspace is stable across objectives, while the magnitude reflects the gradient structure induced by the loss.

5.4 Intervention Probe: Rank-1 Commitment Edit

We next test whether the write-pathway geometry is functionally involved in token commitment. The rank-1 edit from Eq. 11 is evaluated on natural Wikipedia continuations with single-token targets from three concept categories. Each target is tested under *direct*, *indirect*, and *context* elicitation conditions; the direct/indirect ratio measures whether the edit operates at the concept level rather than only on surface forms. Table 2 reports aggregate metrics. The edit substantially lowers target probability while leaving off-concept perplexity close to one. Aligned variants generally show smaller target-logprob drops than their base counterparts, consistent with the alignment-stage geometry being less concentrated in the write pathway. Single-token suppression alone is not decisive, since a chain-rule-only account could also predict effects from editing unembedding directions. The stronger tests are concept-level centroids and direction specificity. The concept direction $\mathbf{u}_{\mathcal{C}}$ is a weighted average of unembedding rows, not a single token row. If the edit were merely token-local, paraphrased elicitations would be much less affected. Instead, among effective-edit model-stage pairs, direct/indirect ratios approach unity across concept categories (Appendix J). Direction controls further support the prediction. We compare the centroid edit with matched-Frobenius edits along a random direction and a direction in the bottom-50 right-singular subspace of W_U . Centroid edits reduce target log-probability by 0.92–3.43 nats across responding checkpoints, while both controls remain within ± 0.02 nats of zero (Appendix K). Thus suppression depends on alignment with the predicted top spectral directions, not merely on editing any direction in W_U space. Two additional analyses support the quantitative boundary of the intervention. First, edit strength decreases as the stable rank of ΔW_U increases (Appendix L), consistent with broad unembedding reorganization decoupling the W_U -derived centroid from the model’s active suppression direction.

Second, contrastive fine-tunes show graded suppression magnitudes that track their write-pathway Π_{pred} ratios (Table 5).

5.5 Cross-Architecture and Feature-Level Bridge

Finally, we extend the probe to architectures where matched alignment-stage checkpoints are unavailable. We measure activation concentration $\text{RSF}_{\text{act}}(\mathbf{h}, \Pi_{\text{pred}})$, the fraction of residual-stream norm lying in the prediction subspace. This is not a weight-delta measurement; it is a complementary activation-level signature of whether prediction-aligned geometry appears in intermediate representations. Table 7 shows a large family-level separation. Autoregressive transformers cluster around $\text{RSF}_{\text{act}} \approx 0.15$ at the median layer and rise through depth, whereas Dream-7B and Mamba remain near 0.01–0.03. A randomly initialized AR baseline sits at the k/d null. Since these models share a terminal softmax output trained with cross-entropy, the separation suggests that architectural differences affect how prediction-gradient structure propagates through intermediate representations. For Dream-7B, the noise level t controls the fraction of positions that supply cross-entropy gradient. Across the five tested noise levels, RSF_{act} decreases monotonically as this gradient density falls ($\rho = -1.00$, $N = 5$; exact two-sided permutation $p = 0.0167$)². Mamba provides a complementary negative case: it shares the AR output projection but lacks the transformer residual-stream pathway through which this geometry accumulates, and accordingly shows low intermediate concentration. In AR transformers, activation-level concentration tracks weight-level write-pathway concentration in 4 of 5 tested models (Appendix M), supporting its use as a cross-architecture proxy.

6 Limitations

The framework is structural rather than quantitative: it identifies the conditions under which each pathway concentrates and the spectral quantities that determine concentration magnitude, but it does not derive observed RSF magnitudes from first principles, and the rank-1 intervention’s quantitative boundary in ΔW_U stable rank is established empirically across the model sample rather than predicted in advance. The within-checkpoint rise–peak–decay trajectory is observed on a single pretraining suite (Pythia, the only public suite with log-spaced checkpoints at the relevant scale); the above-null asymptote replicates across six base architectures in the static results, but the coincidence of the peak with prediction-manifold formation is currently a single-family observation. The cross-architecture extension to DLM and Mamba relies on the activation-level probe alone, since alignment-stage checkpoints are unavailable for these families, and the Dream-7B noise-level relationship rests on $N = 5$ points.

7 Conclusion

Pretraining and alignment deposit their effects in geometrically distinct subspaces of distinct weight matrices. Read-pathway weights (W_Q, W_K) concentrate in the principal subspace of attention input activations under any training objective; write-pathway weights (W_O, W_2) concentrate in the prediction manifold spanned by the top singular vectors of the unembedding only when the loss produces sufficiently sharp per-sample upstream-gradient structure. The asymmetry follows from a structural property of how rank-1 gradient outer products accumulate, combined with a difference in which side carries anisotropy in each pathway: input-side covariance is spiked under any objective, while sharp per-sample upstream-gradient structure is loss-specific. Cross-entropy pretraining is the canonical case where this condition holds on the output side, supplying the upstream-gradient anisotropy that organises the write pathway during pretraining. The within-checkpoint Pythia trajectory identifies the mechanism producing the rise–peak–decay shape of write-pathway concentration: the peak coincides with completion of the prediction manifold’s formation, with the same reorganisation observed simultaneously in mid-stack activation covariance. A graded contrastive-objective control verifies that write-pathway concentration scales with per-sample gradient sharpness rather than collapsing uniformly. A closed-form rank-1 intervention with direction-specificity controls verifies causality and recovers a quantitative boundary tied to unembedding reorganisation.

²Because this is a five-point within-model sweep, we treat the trend as descriptive evidence of a dose response rather than as a standalone inferential result.

References

- Alessandro Achille, Giovanni Paolini, and Stefano Soatto. Where is the information in a deep neural network? *arXiv preprint arXiv:1905.12213*, 2019.
- Shun-ichi Amari. Natural gradient works efficiently in learning. *Neural Computation*, 10(2):251–276, 1998. doi: 10.1162/089976698300017746.
- Shun-ichi Amari, Ryo Karakida, and Masafumi Oizumi. Fisher information and natural gradient learning in random deep networks. In Kamalika Chaudhuri and Masashi Sugiyama, editors, *Proceedings of the Twenty-Second International Conference on Artificial Intelligence and Statistics*, volume 89 of *Proceedings of Machine Learning Research*, pages 694–702. PMLR, 16–18 Apr 2019. URL <https://proceedings.mlr.press/v89/amari19a.html>.
- Nora Belrose, Igor Ostrovsky, Lev McKinney, Zach Furman, Logan Smith, Danny Halawi, Stella Biderman, and Jacob Steinhardt. Eliciting latent predictions from transformers with the tuned lens. *arXiv preprint arXiv:2303.08112*, 2023a.
- Nora Belrose, David Schneider-Joseph, Shauli Ravfogel, Ryan Cotterell, Edward Raff, and Stella Biderman. Leace: Perfect linear concept erasure in closed form. *Advances in Neural Information Processing Systems*, 36:66044–66063, 2023b.
- Trenton Bricken, Adly Templeton, Joshua Batson, Brian Chen, Adam Jermyn, Tom Conerly, Nick Turner, Cem Anil, Carson Denison, Amanda Askell, Robert Lasenby, Yifan Wu, Shauna Kravec, Nicholas Schiefer, Tim Maxwell, Nicholas Joseph, Zac Hatfield-Dodds, Alex Tamkin, Karina Nguyen, Brayden McLean, Josiah E Burke, Tristan Hume, Shan Carter, Tom Henighan, and Christopher Olah. Towards monosemanticity: Decomposing language models with dictionary learning. *Transformer Circuits Thread*, 2023. <https://transformer-circuits.pub/2023/monosemantic-features/index.html>.
- Nelson Elhage, Neel Nanda, Catherine Olsson, Tom Henighan, Nicholas Joseph, Ben Mann, Amanda Askell, Yuntao Bai, Anna Chen, Tom Conerly, Nova DasSarma, Dawn Drain, Deep Ganguli, Zac Hatfield-Dodds, Danny Hernandez, Andy Jones, Jackson Kernion, Liane Lovitt, Kamal Ndousse, Dario Amodei, Tom Brown, Jack Clark, Jared Kaplan, Sam McCandlish, and Chris Olah. A mathematical framework for transformer circuits. *Transformer Circuits Thread*, 2021. <https://transformer-circuits.pub/2021/framework/index.html>.
- Mor Geva, Roei Schuster, Jonathan Berant, and Omer Levy. Transformer feed-forward layers are key-value memories. In *Proceedings of the 2021 Conference on Empirical Methods in Natural Language Processing*, pages 5484–5495, 2021.
- Mor Geva, Avi Caciularu, Kevin Wang, and Yoav Goldberg. Transformer feed-forward layers build predictions by promoting concepts in the vocabulary space. In Yoav Goldberg, Zornitsa Kozareva, and Yue Zhang, editors, *Proceedings of the 2022 Conference on Empirical Methods in Natural Language Processing*, pages 30–45, Abu Dhabi, United Arab Emirates, December 2022. Association for Computational Linguistics. doi: 10.18653/v1/2022.emnlp-main.3. URL <https://aclanthology.org/2022.emnlp-main.3/>.
- Jiwoo Hong, Noah Lee, and James Thorne. Orpo: Monolithic preference optimization without reference model. In *Proceedings of the 2024 Conference on Empirical Methods in Natural Language Processing*, pages 11170–11189, 2024.
- Yen-Chang Hsu, Ting Hua, Sungen Chang, Qian Lou, Yilin Shen, and Hongxia Jin. Language model compression with weighted low-rank factorization. *arXiv preprint arXiv:2207.00112*, 2022.
- Edward J Hu, Yelong Shen, Phillip Wallis, Zeyuan Allen-Zhu, Yuanzhi Li, Shean Wang, Liang Wang, Weizhu Chen, et al. Lora: Low-rank adaptation of large language models. *Iclr*, 1(2):3, 2022.
- Gabriel Ilharco, Marco Tulio Ribeiro, Mitchell Wortsman, Ludwig Schmidt, Hannaneh Hajishirzi, and Ali Farhadi. Editing models with task arithmetic. In *The Eleventh International Conference on Learning Representations*, 2023. URL <https://openreview.net/forum?id=6t0Kwf8-jrj>.

- Ajay Jaiswal, Shiwei Liu, Tianlong Chen, Zhangyang Wang, et al. The emergence of essential sparsity in large pre-trained models: The weights that matter. *Advances in Neural Information Processing Systems*, 36:38887–38901, 2023.
- James Martens and Roger Grosse. Optimizing neural networks with kronecker-factored approximate curvature. In *International conference on machine learning*, pages 2408–2417. PMLR, 2015.
- Charles H Martin and Michael W Mahoney. Implicit self-regularization in deep neural networks: Evidence from random matrix theory and implications for learning. *Journal of Machine Learning Research*, 22(165):1–73, 2021.
- Kevin Meng, David Bau, Alex Andonian, and Yonatan Belinkov. Locating and editing factual associations in gpt. *Advances in neural information processing systems*, 35:17359–17372, 2022a.
- Kevin Meng, Arnab Sen Sharma, Alex Andonian, Yonatan Belinkov, and David Bau. Mass-editing memory in a transformer. *arXiv preprint arXiv:2210.07229*, 2022b.
- Jack Merullo, Carsten Eickhoff, and Ellie Pavlick. Language models implement simple Word2Vec-style vector arithmetic. In Kevin Duh, Helena Gomez, and Steven Bethard, editors, *Proceedings of the 2024 Conference of the North American Chapter of the Association for Computational Linguistics: Human Language Technologies (Volume 1: Long Papers)*, pages 5030–5047, Mexico City, Mexico, June 2024. Association for Computational Linguistics. doi: 10.18653/v1/2024.naacl-long.281. URL <https://aclanthology.org/2024.naacl-long.281/>.
- Eric Mitchell, Charles Lin, Antoine Bosselut, Chelsea Finn, and Christopher D Manning. Fast model editing at scale. *arXiv preprint arXiv:2110.11309*, 2021.
- Neel Nanda, Lawrence Chan, Tom Lieberum, Jess Smith, and Jacob Steinhardt. Progress measures for grokking via mechanistic interpretability. In *The Eleventh International Conference on Learning Representations*, 2023. URL <https://openreview.net/forum?id=9XFSbDPmdW>.
- nostalgebraist. Interpreting GPT: the logit lens. <https://www.lesswrong.com/posts/AcKRB8wDpdaN6v6ru/interpreting-gpt-the-logit-lens>, 2020. Accessed: 2026-04-29.
- Chris Olah, Nick Cammarata, Ludwig Schubert, Gabriel Goh, Michael Petrov, and Shan Carter. Zoom in: An introduction to circuits. *Distill*, 2020. doi: 10.23915/distill.00024.001. <https://distill.pub/2020/circuits/zoom-in>.
- Catherine Olsson, Nelson Elhage, Neel Nanda, Nicholas Joseph, Nova DasSarma, Tom Henighan, Ben Mann, Amanda Askell, Yuntao Bai, Anna Chen, et al. In-context learning and induction heads. *arXiv preprint arXiv:2209.11895*, 2022.
- Varдан Papyan, X. Y. Han, and David L. Donoho. Prevalence of neural collapse during the terminal phase of deep learning training. *CoRR*, abs/2008.08186, 2020. URL <https://arxiv.org/abs/2008.08186>.
- Kiho Park, Yo Joong Choe, Yibo Jiang, and Victor Veitch. The geometry of categorical and hierarchical concepts in large language models, 2025. URL <https://arxiv.org/abs/2406.01506>.
- Rafael Rafailov, Archit Sharma, Eric Mitchell, Christopher D Manning, Stefano Ermon, and Chelsea Finn. Direct preference optimization: Your language model is secretly a reward model. *Advances in neural information processing systems*, 36:53728–53741, 2023.
- Shauli Ravfogel, Yanai Elazar, Hila Gonen, Michael Twiton, and Yoav Goldberg. Null it out: Guarding protected attributes by iterative nullspace projection. In Dan Jurafsky, Joyce Chai, Natalie Schluter, and Joel Tetreault, editors, *Proceedings of the 58th Annual Meeting of the Association for Computational Linguistics*, pages 7237–7256, Online, July 2020. Association for Computational Linguistics. doi: 10.18653/v1/2020.acl-main.647. URL <https://aclanthology.org/2020.acl-main.647/>.
- Shauli Ravfogel, Michael Twiton, Yoav Goldberg, and Ryan D Cotterell. Linear adversarial concept erasure. In *International Conference on Machine Learning*, pages 18400–18421. PMLR, 2022.

- Nina Rimsky, Nick Gabrieli, Julian Schulz, Meg Tong, Evan Hubinger, and Alexander Turner. Steering llama 2 via contrastive activation addition. In Lun-Wei Ku, Andre Martins, and Vivek Srikumar, editors, *Proceedings of the 62nd Annual Meeting of the Association for Computational Linguistics (Volume 1: Long Papers)*, pages 15504–15522, Bangkok, Thailand, August 2024. Association for Computational Linguistics. doi: 10.18653/v1/2024.acl-long.828. URL <https://aclanthology.org/2024.acl-long.828/>.
- Pratyusha Sharma, Jordan T Ash, and Dipendra Misra. The truth is in there: Improving reasoning in language models with layer-selective rank reduction. *arXiv preprint arXiv:2312.13558*, 2023.
- Anton Sinitin, Vsevolod Plokhotnyuk, Dmitry Pyrkin, Sergei Popov, and Artem Babenko. Editable neural networks. In *International Conference on Learning Representations*, 2020. URL <https://openreview.net/forum?id=HJedXaEtvS>.
- Daniel Soudry, Elad Hoffer, Mor Shpigel Nacson, Suriya Gunasekar, and Nathan Srebro. The implicit bias of gradient descent on separable data. *J. Mach. Learn. Res.*, 19(1):2822–2878, January 2018. ISSN 1532-4435.
- Alexander Matt Turner, Lisa Thiergart, Gavin Leech, David Udell, Juan J Vazquez, Ulisse Mini, and Monte MacDiarmid. Steering language models with activation engineering. *arXiv preprint arXiv:2308.10248*, 2023.
- Kevin Ro Wang, Alexandre Variengien, Arthur Conmy, Buck Shlegeris, and Jacob Steinhardt. Interpretability in the wild: a circuit for indirect object identification in GPT-2 small. In *The Eleventh International Conference on Learning Representations*, 2023. URL <https://openreview.net/forum?id=NpsVSN6o4u1>.
- Peihao Wang, Ruisi Cai, Zhen Wang, Hongyuan Mei, Qiang Liu, Pan Li, and Zhangyang Wang. nabra-reasoner: Llm reasoning via test-time gradient descent in latent space. *arXiv preprint arXiv:2603.04948*, 2026.
- Mitchell Wortsman, Gabriel Ilharco, Samir Ya Gadre, Rebecca Roelofs, Raphael Gontijo-Lopes, Ari S Morcos, Hongseok Namkoong, Ali Farhadi, Yair Carmon, Simon Kornblith, et al. Model soups: averaging weights of multiple fine-tuned models improves accuracy without increasing inference time. In *International conference on machine learning*, pages 23965–23998. PMLR, 2022.
- Robert Wu and Vardan Papyan. Linguistic collapse: Neural collapse in (large) language models. In A. Globerson, L. Mackey, D. Belgrave, A. Fan, U. Paquet, J. Tomczak, and C. Zhang, editors, *Advances in Neural Information Processing Systems*, volume 37, pages 137432–137473. Curran Associates, Inc., 2024a. doi: 10.52202/079017-4366. URL https://proceedings.neurips.cc/paper_files/paper/2024/file/f88cc8930b47a45ec4733123bf3039b9-Paper-Conference.pdf.
- Robert Wu and Vardan Papyan. Linguistic collapse: Neural collapse in (large) language models. *Advances in Neural Information Processing Systems*, 37:137432–137473, 2024b.
- Zhengxuan Wu, Aryaman Arora, Zheng Wang, Atticus Geiger, Dan Jurafsky, Christopher D. Manning, and Christopher Potts. Reft: Representation finetuning for language models, 2024. URL <https://arxiv.org/abs/2404.03592>.
- Shusheng Xu, Wei Fu, Jiakuan Gao, Wenjie Ye, Weilin Liu, Zhiyu Mei, Guangju Wang, Chao Yu, and Yi Wu. Is dpo superior to ppo for llm alignment? a comprehensive study, 2024. URL <https://arxiv.org/abs/2404.10719>.
- Prateek Yadav, Derek Tam, Leshem Choshen, Colin Raffel, and Mohit Bansal. TIES-merging: Resolving interference when merging models. In *Thirty-seventh Conference on Neural Information Processing Systems*, 2023. URL <https://openreview.net/forum?id=xtaX3WyCj1>.
- Zhilin Yang, Zihang Dai, Ruslan Salakhutdinov, and William W. Cohen. Breaking the softmax bottleneck: A high-rank RNN language model. In *International Conference on Learning Representations*, 2018. URL <https://openreview.net/forum?id=HkwZSG-CZ>.

Table 3: Mixed-effects test on the diagonal contrast (predicted elevation: Π_{input} on reads, Π_{pred} on writes) versus cross-projector control. Architecture-level paired Wilcoxon: one observation per architecture, $N = 7$.

Pathway	β	z	p (mixed-eff.)	p (Wilcoxon)
Read	+0.98	5.89	4×10^{-9}	0.008
Write	-0.18	-6.81	1×10^{-11}	1.000

Table 4: Pythia within-checkpoint trajectory. $\text{RSF}(W^{(t)}, \Pi_{\text{pred}}^{(t)})/(k/d)$ aggregated across W_O and W_2 , with bootstrap CI over (layers \times matrices). The peak coincides with stabilisation of $\Pi_{\text{pred}}^{(t)}$.

Step	RSF / null [95% CI]	$\cos \angle(\Pi_{\text{pred}}^{(0)}, \Pi_{\text{pred}}^{(t)})$
16	1.00 [1.00, 1.00]	1.000
256	1.05 [1.04, 1.06]	0.721
1000	2.52 [2.17, 2.89]	0.149
4000	2.08 [1.85, 2.33]	0.141
16000	1.59 [1.47, 1.71]	0.138
64000	1.38 [1.30, 1.47]	0.135
143000	1.30 [1.24, 1.38]	0.135

Yang You, Jing Li, Sashank Reddi, Jonathan Hseu, Sanjiv Kumar, Srinadh Bhojanapalli, Xiaodan Song, James Demmel, Kurt Keutzer, and Cho-Jui Hsieh. Large batch optimization for deep learning: Training bert in 76 minutes. *arXiv preprint arXiv:1904.00962*, 2019.

Le Yu, Bowen Yu, Haiyang Yu, Fei Huang, and Yongbin Li. Language models are super mario: Absorbing abilities from homologous models as a free lunch. In *Forty-first International Conference on Machine Learning*, 2024.

Lei Yu, Virginie Do, Karen Hambardzumyan, and Nicola Cancedda. Robust llm safeguarding via refusal feature adversarial training, 2025. URL <https://arxiv.org/abs/2409.20089>.

Andy Zou, Long Phan, Sarah Chen, James Campbell, Phillip Guo, Richard Ren, Alexander Pan, Xuwang Yin, Mantas Mazeika, Ann-Kathrin Dombrowski, et al. Representation engineering: A top-down approach to ai transparency. *arXiv preprint arXiv:2310.01405*, 2023.

A Tables from the paper

B Experimental Setup

We evaluate weight-space geometry on matched base-aligned checkpoint pairs whenever available. The main static-RSF analysis covers seven base architectures and their SFT, DPO, or ORPO variants: Llama-3.2-3B, Llama-3-8B, Llama-3.1-8B/Tulu, OLMo-2-7B, Qwen2.5-3B, Qwen2.5-7B, and Mistral-7B. Alignment deltas are computed as $\Delta W = W_{\text{aligned}} - W_{\text{base}}$ for single-stage alignment, and as $\Delta W = W_{\text{DPO}} - W_{\text{SFT}}$ when we isolate the second stage of a two-stage pipeline. Full checkpoint identifiers and omitted unavailable pairs are listed in Table 29.

For all RSF measurements we use rank $k = 50$ projectors and report ratios relative to the isotropic k/d null. Values are averaged over layers and over matrices within each pathway: W_O, W_2 for writes and W_Q, W_K for reads. The internal-sublayer analysis additionally reports W_V and W_1 . Π_{pred} is computed from the top right singular vectors of the unembedding W_U . Activation-based projectors are computed from forward passes on WikiText-2 by default: Π_{input} from residual-stream PCA at each layer, and Π_{behav} from PCA of final-layer activation differences $\mathbf{h}_{\text{aligned}} - \mathbf{h}_{\text{base}}$. Appendix C.2 repeats the analysis on C4, OASST1, and Alpaca, and Appendix C.3 compares base-model and aligned-model activation projectors.

To test objective dependence, we use contrastive fine-tuning pairs: MiniLM-L6, MPNet-base, GTE-Qwen2-1.5B, and E5-Mistral-7B, with Mistral-7B-Instruct-v0.1 as a matched SFT comparison. To

Table 5: RSF ratios on $\Delta W = W_{\text{contrastive}} - W_{\text{backbone}}$. Encoder InfoNCE and GTE-Qwen2 collapse on the write side; E5-Mistral retains partial concentration. Read-pathway elevation persists across all pairs. SFT baseline included for comparison.

Pair	Family	Write : Π_{pred}	Read : Π_{input}
MiniLM-L6 (MLM \rightarrow SBERT)	encoder	1.07	1.36
MPNet-base (MLM \rightarrow SBERT)	encoder	1.07	1.92
GTE-Qwen2-1.5B (CE \rightarrow InfoNCE)	decoder	1.10	1.28
E5-Mistral-7B (CE \rightarrow InfoNCE)	decoder	1.71	1.28
SFT alignment (Mistral)	decoder	1.13	1.77

Table 6: Activation-level concentration across architectures. RSF_{act} at the median layer; the trajectory through depth is monotone-rising in AR and flat in DLM/Mamba. Random-init AR sits at the k/d null. Dream-7B noise levels t control the fraction of masked positions seen at evaluation.

Family	Model	RSF_{act}
AR	Qwen2.5-7B	0.163
	Llama-3.1-8B	0.157
	Qwen2.5-0.5B	0.156
	Gemma-2-2B	0.149
DLM (Dream-7B)	$t = 0.1$	0.029
	$t = 0.3$	0.028
	$t = 0.5$	0.025
	$t = 0.7$	0.019
	$t = 0.9$	0.010
SSM	Mamba-370M	0.010
Random-init AR	Llama-3.2-3B	0.016 ($\approx k/d$)

test pretraining dynamics, we use the public Pythia checkpoint trajectory and recompute both $W^{(t)}$ and $\Pi_{\text{pred}}^{(t)}$ at each training step. For cross-architecture activation probes, where matched alignment deltas are unavailable, we report $\text{RSF}_{\text{act}}(\mathbf{h}, \Pi_{\text{pred}})$ on autoregressive transformers, Dream-7B across five noise levels, Mamba-370M, and a randomly initialized autoregressive baseline.

The rank-1 write-pathway intervention is evaluated on natural Wikipedia continuation prompts with single-token targets from three concept clusters. For each prompt we report target probability before and after the edit, target log-probability change, held-out continuation log-probability change, and perplexity ratio on an off-concept reference corpus. Because centroid construction depends on single-token coverage, tokenizer coverage is reported separately and Mistral is evaluated on its single-token subset where appropriate (Appendix K).

For the static RSF analysis, the unit of observation is a (model-stage, layer, matrix-tier, projector) value $y_i = \log(\text{RSF}_i/(k/d))$. We fit

$$y_i = \beta_0 + \beta_1 \text{Diag}_i + \beta_2 \text{Pathway}_i + \beta_3 (\text{Diag}_i \times \text{Pathway}_i) + b_{\text{arch}[i]} + \epsilon_i,$$

where Diag indicates the predicted pathway-projector pairing, Π_{input} for reads and Π_{pred} for writes, and $b_{\text{arch}} \sim \mathcal{N}(0, \sigma_{\text{arch}}^2)$ is a random intercept for base architecture. Models are fit in Python using `statsmodels MixedLM`; p -values use Wald z tests. We also report an architecture-level paired Wilcoxon test in which each base architecture contributes one aggregated contrast, providing a conservative nonparametric check on the mixed-effects result.

C Robustness checks for the static dissociation

C.1 Robustness to Choice of k

The main analysis fixes $k = 50$ for all projectors. Table 9 reports the read-pathway Π_{input} ratio under three choices of k on three representative SFT models. The asymmetric write/read dissociation is preserved across the range.

Table 7: Residual-stream concentration across architectures. FR (rad) is Fisher–Rao distance from the output distribution to the nearest simplex vertex, $\arccos(\sqrt{p_{\max}})$; theoretical maximum is $\arccos(1/\sqrt{V}) \approx 1.568$. RSF_{act} is computed with $k = 50$ at the median layer. Dream-7B is reported at five noise levels t , where the fraction of masked positions equals t . Spearman correlations across the Dream rows: $\rho(t, \text{FR}) = +1.00$, $\rho(t, \text{RSF}_{\text{act}}) = -1.00$.

Family	Model	FR (rad)	RSF_{act}	Commit depth
AR	Qwen2.5-0.5B	0.836	0.156	19.2
	Qwen2.5-7B	0.718	0.163	17.8
	Llama-3.1-8B	0.747	0.157	18.5
	Gemma-2-2B	0.787	0.149	19.7
DLM	Dream-7B ($t = 0.1$)	0.665	0.029	21.3
	Dream-7B ($t = 0.3$)	0.695	0.028	21.8
	Dream-7B ($t = 0.5$)	0.753	0.025	22.1
	Dream-7B ($t = 0.7$)	0.939	0.019	23.0
	Dream-7B ($t = 0.9$)	1.211	0.010	23.4
SSM	Mamba-370M	0.846	0.010	20.3

Table 8: Model checkpoints used in the static alignment-delta analysis. A dash indicates that no matched checkpoint was used. Two-stage DPO pipelines are evaluated both against the base model when appropriate and against the SFT checkpoint to isolate the DPO contribution.

Group	Base	SFT	DPO	ORPO
Llama-3B	Llama-3.2-3B	Llama-3.2-3B-Instruct	tanliboy/Llama-3.2-3B-DPO	–
Llama-8B	Meta-Llama-3-8B	Meta-Llama-3-8B-Instruct	OpenHermes-DPO	Llama-3-8B-Orpo-v0.1
Tulu-8B	Llama-3.1-8B	Tulu-3-8B-SFT	Tulu-3-8B-DPO	–
OLMo-7B	OLMo-2-7B	OLMo-2-7B-SFT	OLMo-2-7B-DPO	–
Qwen-3B	Qwen2.5-3B	Qwen2.5-3B-Instruct	Qwen2.5-3B-dpo-tuned	Qwen2.5-3B-orpo
Qwen-7B	Qwen2.5-7B	Qwen2.5-7B-Instruct	Qwen2.5-7B-DPO-main	–
Mistral-7B	Mistral-7B-v0.1	Mistral-7B-Instruct-v0.1	zephyr-7b-beta	Mistral-7B-ORPO-beta

C.2 Calibration Sensitivity of Pi input

The main analysis constructs Π_{input} from activations on WikiText-2. Table 10 reports the read-pathway ratio under three additional calibration sources spanning the range from general-domain text to instruction-response data.

The ordering across sources is consistent across models: $\text{WikiText-2} < \text{C4} < \text{Alpaca} \approx \text{OASST1}$, with instruction-response sources giving higher ratios than general-domain prose. This tracks the prediction that Π_{input} better captures alignment-delta mass when the calibration distribution approximates the alignment training distribution. Qwen2.5-7B shows substantially lower calibration sensitivity than the other two families (range 0.30 vs 0.85–1.04), consistent with its narrower residual-stream geometry. The WikiText-2 ratios reported in the main text are conservative lower bounds.

C.3 Robustness of Pi input to Source Model

The main analysis builds Π_{input} from base-model activations. Section 4.3’s read condition refers to activation covariance during alignment training specifically, raising the question of whether base-model activations are an adequate proxy. Table 11 reports the per-model comparison.

The differences are within bootstrap uncertainty of either measurement and the principal-angle cosines are high enough that the two projectors are operationally equivalent. The base-model protocol used in the main analysis is therefore a defensible proxy. The two models show differences in opposite directions (Llama drops, Mistral rises), consistent with the differences reflecting calibration variability rather than systematic base-vs-aligned drift.

Table 9: Read-pathway Π_{input} ratio under three choices of subspace rank k . Bootstrap CIs over layers. The dissociation is preserved throughout, with magnitude varying smoothly with k .

Model	$k = 32$	$k = 50$	$k = 64$
Llama-3.2-3B SFT	2.30 [2.15, 2.46]	2.15 [2.01, 2.30]	2.05 [1.92, 2.18]
Mistral-7B SFT	2.78 [2.51, 3.07]	2.59 [2.34, 2.85]	2.45 [2.21, 2.69]
Qwen2.5-7B SFT	1.91 [1.74, 2.09]	1.76 [1.61, 1.93]	1.65 [1.51, 1.81]

Table 10: Read-pathway RSF ratio (averaged across W_Q, W_K and across all layers) relative to the k/d null under four calibration sources. The write/read asymmetry is preserved under every source; magnitude scales with proximity of the calibration distribution to the alignment training distribution. The ‘‘Range’’ column reports the spread across sources; ‘‘Mean cos’’ is the mean principal-angle cosine between projectors across sources.

Model	WikiText-2	C4	OASST1	Alpaca	Range	Mean cos
Llama-3-8B	3.36	3.83	4.21	4.01	0.85	0.40
Mistral-7B	2.22	2.95	3.26	3.17	1.04	0.41
Qwen2.5-7B	1.82	1.87	2.12	2.08	0.30	0.47

C.4 Internal-sublayer matrices

The write/read taxonomy in Section 3 partitions the six transformer weight matrices by their position relative to the residual stream. W_Q and W_K read directly from it; W_O and W_2 write directly into it; W_V and W_1 are internal to their respective sublayers and couple to the residual stream only through a downstream matrix (W_O or W_2). The chain rule predicts that W_V and W_1 inherit read-pathway geometry, their row spaces are constrained by the activation distribution $\mathbf{h}_t^{(\ell)}$ they take as input, but not write-pathway geometry, because their column spaces do not couple directly to $\text{row}(W_U)$. The prediction is graded: direct reads (W_Q, W_K) are full outer-product gradients of the residual stream, while internal reads are outer products with inputs that pass through additional intermediate matrices, reducing the clean concentration structure in Π_{input} .

Table 12 reports RSF ratios for $W_V, W_1^{\text{gate}},$ and W_1^{up} across all five model groups and alignment stages. Π_{pred} ratios cluster near the k/d null: means 1.048 (W_V), 1.055 (W_1^{gate}), 1.050 (W_1^{up}), compared to 1.20 for W_2 and 1.08 for W_O in the main analysis. Π_{input} ratios are elevated but uniformly weaker than the residual-stream-adjacent reads: means 1.376, 1.369, 1.316 respectively, compared to ≈ 1.80 for W_Q and W_K in Table 15. The pattern extends the two-pathway dissociation into a three-tier hierarchy: residual-stream-adjacent writes concentrate in Π_{pred} , residual-stream-adjacent reads concentrate strongly in Π_{input} , and internal-sublayer reads concentrate moderately in Π_{input} without Π_{pred} structure. The attenuation of internal reads relative to direct reads follows from chain-rule composition: W_V ’s gradient is the outer product $\delta_V \mathbf{h}^\top$ after multiplication by W_O downstream, which mixes directions and reduces the clean outer-product concentration in Π_{input} ; W_1 ’s gradient is similarly mediated by the MLP nonlinearity and W_2 .

A small systematic pattern appears at the top of the stack across models: both Π_{pred} and Π_{input} ratios rise at the final layer by 0.05–0.2. This is compatible with a weak chain-rule leakage: at the layer immediately preceding the unembedding, internal matrices sit close enough to W_U that a small fraction of $\text{row}(W_U)$ structure propagates into their gradients. The effect is small and does not disturb the pattern in the layer-averaged aggregates.

D Full Per-Model RSF Values

Table 13 reports per-model, per-stage RSF ratios relative to the k/d null, layer-averaged over W_O, W_2 (write) and W_Q, W_K (read). Panel A reports single-stage alignment (ΔW vs base). Panel B reports the isolated DPO contribution on two-stage pipelines (ΔW vs SFT) where the SFT-vs-base component is dominant in the ΔW -vs-base measurement.

Table 11: Read-pathway RSF ratio computed with Π_{input} built from base-model versus aligned-model activations on WikiText-2. Bootstrap CIs over layers (5000 resamples). Mean principal-angle cosine measures the overlap between the two projectors per layer, averaged over layers.

Model	From base	From aligned	Difference	cos(angles)
Llama-3.2-3B	1.808 [1.755, 1.862]	1.744 [1.697, 1.792]	-0.064 [-0.087, -0.041]	0.889
Mistral-7B	1.769 [1.648, 1.927]	1.808 [1.668, 1.995]	+0.038 [+0.015, +0.073]	0.886

Table 12: Internal-sublayer RSF ratios (relative to the k/d null) for W_V , W_1^{gate} , and W_1^{up} across all model-stage pairs. Layer-averaged. Bold entries indicate ratios > 1.3 . Π_{pred} ratios cluster near null (1.05 mean across the sample); Π_{input} ratios are uniformly elevated but weaker than the residual-stream-adjacent reads W_Q, W_K in Table 15. The pattern extends the two-pathway dissociation into the three-tier hierarchy described in the main text.

Model	Stage	Π_{pred}		Π_{input}	
		W_V	$W_1^{\text{gate/up}}$	W_V	$W_1^{\text{gate/up}}$
Llama-3.2-3B	SFT	1.02	1.08 / 1.08	1.15	1.31 / 1.25
	DPO	1.25	1.23 / 1.22	2.07	1.98 / 1.91
Llama-3-8B	SFT	0.98	1.02 / 1.01	1.37	1.46 / 1.37
	DPO	1.09	— [†]	1.60	— [†]
	ORPO	1.06	1.02 / 1.04	1.14	1.09 / 1.11
Llama-3.1-8B (Tulu)	SFT	0.98	1.03 / 1.01	1.48	1.51 / 1.43
	DPO*	0.98	1.03 / 1.02	1.48	1.51 / 1.43
Mistral-7B	SFT	1.04	1.11 / 1.09	1.31	1.40 / 1.34
	DPO	1.10	1.11 / 1.10	1.39	1.44 / 1.35
	ORPO	1.04	1.03 / 1.04	1.40	1.17 / 1.25
Qwen2.5-3B	SFT	1.07	1.07 / 1.07	1.12	1.19 / 1.14
	ORPO	1.07	1.06 / 1.06	1.23	1.29 / 1.23
Qwen2.5-7B	SFT	1.01	1.03 / 1.03	1.27	1.31 / 1.24
	DPO*	1.01	1.03 / 1.03	1.27	1.31 / 1.24
<i>Sample mean</i>		1.05	1.06 / 1.05	1.38	1.34 / 1.30

[†] $\Delta W_1 \approx 0$ for Llama-3-8B ORPO checkpoint; the DPO row inherits the same near-zero MLP delta. * DPO for Tulu-8B and Qwen2.5-7B is trained on top of SFT and the ΔW vs base is dominated by the SFT component, matching the pattern in Table 12.

E Objective Control: Full Analysis

We report the complete results of the contrastive fine-tuning control summarised in Section 5.3. The test isolates the effect of the training objective by measuring RSF on ΔW between a sentence-transformers model and its CE-pretrained backbone. Two model pairs are used. The MiniLM-L6 pair is `nreimers/MiniLM-L6-H384-uncased` as backbone (MLM-pretrained BERT-family, $d = 384$, $L = 6$) and `sentence-transformers/all-MiniLM-L6-v2` as the fine-tuned version. The MPNet-base pair is `microsoft/mpnet-base` as backbone (permutation-LM pretrained, $d = 768$, $L = 12$) and `sentence-transformers/all-mpnet-base-v2` as the fine-tuned version. Both fine-tuning runs use InfoNCE loss on large-scale sentence-pair data; we use the tied input embedding matrix as the W_U proxy for construction of Π_{pred} .

RSF ratios on the contrastive delta Table 16 reports RSF ratios relative to the k/d null under both projectors, averaged across layers. For the write pathway, both models show Π_{pred} ratios within 10% of null, an order of magnitude closer to null than the SFT and DPO alignment deltas in the main analysis. Read-pathway ratios under Π_{input} are elevated (consistent with the objective-agnostic chain-rule argument of Section 4), and ratios under Π_{pred} are moderately elevated.

Subspace overlap between Π_{pred} and Π_{input} A potential concern is that the read-pathway Π_{pred} elevation reflects geometric overlap between the two projectors in encoder-only models rather than

Table 13: Per-model layer-averaged RSF ratios. Bold entries indicate ratios > 1.3 . Panel A: single-stage alignment vs base. Panel B: two-stage pipelines, with DPO isolated from SFT. The $\text{DPO} \geq \text{SFT}$ ordering predicted by Section 4 holds throughout. “srank” is the stable rank of ΔW_U .

Model	Stage	Π_{pred}		Π_{input}		Π_{behav}		srank
		Wr	Rd	Wr	Rd	Wr	Rd	
<i>Panel A. Single-stage alignment (vs base)</i>								
Llama-3.2-3B	SFT	1.07	1.25	1.17	2.15	1.10	1.34	6.1
	DPO	1.21	1.42	1.45	2.67	1.18	1.40	1.4
Llama-3-8B	SFT	1.03	1.02	1.28	3.14	1.04	1.11	6.0
	ORPO	1.12	1.05	1.39	1.33	1.17	1.07	— [†]
Tülu-3-8B	SFT	1.06	1.01	1.29	2.17	1.04	1.07	12.1
	DPO*	1.06	1.02	1.30	2.18	1.04	1.07	12.1
OLMo-2-7B	SFT	1.11	1.07	1.33	1.71	1.11	1.07	15.4
	DPO*	1.11	1.07	1.33	1.70	1.11	1.07	15.4
Qwen2.5-3B	SFT	1.07	1.13	1.14	1.59	1.05	1.06	1.8
	ORPO	1.10	1.13	1.22	1.79	1.09	1.08	1.8
Qwen2.5-7B	SFT	1.10	1.01	1.19	1.76	1.01	1.00	2.5
Mistral-7B	SFT	1.13	1.07	1.26	2.59	1.10	1.09	10.8
	DPO	1.18	1.12	1.29	3.14	1.09	1.17	25.1
	ORPO	1.03	1.02	1.25	1.22	1.12	1.00	31.9
<i>Panel B. Two-stage pipelines: DPO vs SFT</i>								
Tülu-3-8B	DPO/SFT	1.15	1.06	1.66	2.08	1.07	1.06	163.6
OLMo-2-7B	DPO/SFT	1.29	1.29	1.70	2.67	1.18	1.21	78.1
Mean (Panel A)		1.08	1.10	1.25	2.05	1.09	1.11	

[†] $\Delta W_U \approx 0$ for Llama-3-8B ORPO. * DPO for Tülu-3-8B and OLMo-2 is trained on top of SFT; the ΔW vs base is dominated by the SFT component (see Panel B for the isolated DPO contribution).

Table 14: Raw RSF values (layer-averaged) and null baselines k/d . Complement to Table 13.

Model	Stage	Π_{pred}		Π_{input}		Π_{behav}		k/d
		Wr	Rd	Wr	Rd	Wr	Rd	
Llama-3.2-3B	SFT	.018	.021	.019	.035	.018	.022	.0163
	DPO	.020	.024	.024	.044	.020	.023	.0163
Llama-3-8B	SFT	.013	.012	.016	.038	.013	.014	.0122
	ORPO	.013	.013	.017	.016	.015	.013	.0122
Qwen2.5-7B	SFT	.015	.014	.017	.025	.014	.014	.0140
Qwen2.5-3B	SFT	.026	.028	.028	.039	.026	.026	.0244
	ORPO	.027	.028	.030	.044	.027	.027	.0244
Mistral-7B	SFT	.014	.013	.016	.032	.013	.013	.0122
	DPO	.014	.014	.016	.039	.013	.014	.0122
	ORPO	.013	.012	.015	.016	.013	.012	.0122

structure in the delta itself. Encoder models have substantially smaller hidden dimensions than the decoder models of the main analysis ($d = 384\text{-}768$ versus $d = 3072\text{-}8192$), so the top- k singular subspace of the unembedding and the principal subspace of residual-stream activations can in principle overlap by larger fractions. We test this directly by computing the mean principal-angle cosine between the two k -dimensional bases per layer. For MiniLM-L6 the mean cosine is 0.43 (range 0.41-0.46); for MPNet-base the mean is 0.26 (range 0.24-0.31). Both values are well below the threshold for treating the subspaces as interchangeable, and the MPNet subspaces are in fact close to orthogonal. The read-pathway Π_{pred} elevation is therefore not reducible to trivial subspace overlap.

Observed vs. overlap-predicted elevation A quantitative form of the overlap question is whether the observed read-pathway Π_{pred} ratio is accounted for by projection of the Π_{input} concentration through subspace overlap. Let $f = \|\Pi_{\text{pred}}^\top \Pi_{\text{input}}\|_F^2 / k$ be the fraction of Π_{pred} that lies in Π_{input} . If ΔW has read-pathway concentration $r_{\text{inp}}/\text{null}$ in Π_{input} and no additional structure in Π_{pred} beyond

Table 15: RSF of alignment deltas as multiples of the null baseline k/d ($k=50$). **Write:** W_O, W_2 ; **Read:** W_Q, W_K . Layer-averaged. Ratios > 1.3 in **bold**. Panel A: single-stage alignment ($\Delta\mathbf{W}$ vs base). Panel B: two-stage pipelines, with DPO isolated from SFT ($\Delta\mathbf{W}$ vs SFT).

Model	Stage	Π_{pred}		Π_{input}		Π_{behav}		srank
		Wr	Rd	Wr	Rd	Wr	Rd	
<i>Panel A. Single-stage alignment (vs base)</i>								
Llama-3.2-3B	SFT	1.07	1.25	1.17	2.15	1.10	1.34	6.1
	DPO	1.21	1.42	1.45	2.67	1.18	1.40	1.4
Llama-3-8B	SFT	1.03	1.02	1.28	3.14	1.04	1.11	6.0
	ORPO	1.12	1.05	1.39	1.33	1.17	1.07	$-\dagger$
Llama-3.1-8B (Tülu)	SFT	1.06	1.01	1.29	2.17	1.04	1.07	12.1
	DPO*	1.06	1.02	1.30	2.18	1.04	1.07	12.1
OLMo-2-7B	SFT	1.11	1.07	1.33	1.71	1.11	1.07	15.4
	DPO*	1.11	1.07	1.33	1.70	1.11	1.07	15.4
Qwen2.5-3B	SFT	1.07	1.13	1.14	1.59	1.05	1.06	1.8
	ORPO	1.10	1.13	1.22	1.79	1.09	1.08	1.8
Qwen2.5-7B	SFT	1.10	1.01	1.19	1.76	1.01	1.00	2.5
Mistral-7B	SFT	1.13	1.07	1.26	2.59	1.10	1.09	10.8
	DPO	1.18	1.12	1.29	3.14	1.09	1.17	25.1
	ORPO	1.03	1.02	1.25	1.22	1.12	1.00	31.9
<i>Panel B. Two-stage pipelines: DPO vs SFT (isolated contribution)</i>								
Llama-3.1-8B (Tülu)	DPO/SFT	1.15	1.06	1.66	2.08	1.07	1.06	163.6
OLMo-2-7B	DPO/SFT	1.29	1.29	1.70	2.67	1.18	1.21	78.1
<i>Mean (Panel A)</i>		1.08	1.10	1.25	2.05	1.09	1.11	

$\dagger \Delta W_U \approx 0$ for Llama-3-8B ORPO. * DPO for Tülu and OLMo-2 is trained on top of SFT; the $\Delta\mathbf{W}$ vs base is dominated by the SFT component. See Panel B for the isolated DPO contribution. Llama-3-8B DPO omitted ($\|\Delta\mathbf{W}\| < 10^{-8}$). Qwen2.5-7B DPO omitted (identical to SFT at 4 decimal places).

Table 16: RSF ratios (relative to k/d null) for the contrastive fine-tuning delta $\Delta W = W_{\text{SBERT}} - W_{\text{backbone}}$, averaged across layers. Write-pathway Π_{pred} ratios remain near null; read-pathway Π_{input} ratios are elevated in line with the chain-rule prediction of Section 4. The $M_1^W @ \ell^*$ column is zero by construction and serves as an implementation check.

Pair	Projector	W_O write	W_2 write	W_Q read	W_K read	Write mean	Read mean
MiniLM-L6	Π_{pred}	1.05	1.08	1.27	1.33	1.07	1.30
	Π_{input}	0.92	1.00	1.31	1.41	0.96	1.36
MPNet-base	Π_{pred}	1.01	1.08	1.22	1.20	1.05	1.21
	Π_{input}	1.04	1.11	1.81	2.03	1.07	1.92

what this concentration carries through overlap, the expected Π_{pred} ratio is

$$\hat{r}_{\text{pred}}/\text{null} = f \cdot r_{\text{inp}}/\text{null} + (1 - f). \quad (13)$$

Comparing the observed ratio to \hat{r}_{pred} yields a residual that measures the Π_{input} -independent Π_{pred} concentration of the delta.

Table 17 reports observed, predicted, and residual values. The observed ratio exceeds the overlap prediction in both cases, by +0.20 for MiniLM and +0.12 for MPNet. The residuals are not large in absolute terms, but they are substantial relative to the low overlap fractions involved (for MPNet, $f = 0.10$, so the prediction from overlap alone is almost entirely the null).

Interpretation The write-pathway result is unambiguous. Write-pathway Π_{pred} ratios near null under a contrastive fine-tuning objective falsify the hypothesis that Π_{pred} concentration in the write pathway is a generic property of backpropagation through W_U . The proposed account, which ties

Table 17: Observed read-pathway Π_{pred} ratio vs. the ratio predicted by subspace-overlap propagation of Π_{input} concentration. Residual > 0 indicates the delta has Π_{pred} structure not reducible to Π_{input} concentration alone.

Pair	Overlap f	Observed	Predicted	Residual
MiniLM-L6	0.26	1.30	1.10	+0.20
MPNet-base	0.10	1.21	1.09	+0.12

the concentration to the vertex-attractor structure of the loss gradient, is the remaining candidate explanation consistent with the data.

The read-pathway residual admits a coherent interpretation within the framework. InfoNCE over a batch of N sentence pairs selects one correct match per sample, producing a gradient that has a distinguished target direction even without the strict vertex fixed points of one-hot cross-entropy. The per-sample contrastive structure acts as a weakened vertex attractor: it is not directed toward a fixed vertex on the $(V - 1)$ -simplex, but each sample has a single correct target whose score the loss is minimising against $N - 1$ negatives. The prediction sharpens accordingly: Π_{pred} concentration should scale with the vertex-like structure of the loss gradient, from strong concentration under strict CE to zero under objectives with no distinguished per-sample target. Contrastive objectives sit between these extremes, which matches the residuals observed here. The read pathway is affected because its chain-rule gradient (Section 4) depends on $\delta_Q^{(\ell)}$, which inherits directional structure from the loss gradient at the logits; objectives with stronger vertex-like structure in the logit gradient propagate stronger Π_{pred} alignment to the read-pathway weights.

Summary The objective control supports the specific prediction over the depth-dependent alternative for the write pathway (the critical test) and refines the prediction for the read pathway. Π_{pred} concentration is objective-dependent rather than architecture-dependent: contrastive fine-tuning produces near-null write-pathway concentration and modest, overlap-exceeding read-pathway concentration, in both cases consistent with InfoNCE’s weakened vertex-attractor structure.

F Cross-Architecture Validation

The conditions of Section 4.3 are stated for any model with a softmax output, cross-entropy loss, and a residual stream through which gradient pressure can accumulate. Autoregressive transformers, masked diffusion language models (DLMs), and state-space models (SSMs) share the terminal structure but differ in how gradient pressure propagates to intermediate representations. This appendix reports a residual-stream concentration measurement across the three architectural families, providing a falsification test of the propagation argument that does not require matched aligned-versus-base checkpoints.

F.1 Activation-Level RSF

We define an activation-level analogue of the weight-space RSF used in the main text. For residual-stream activations $\mathbf{h} \in \mathbb{R}^d$ collected from a calibration corpus, let Π_{pred} denote the projector onto the top- k right singular subspace of W_U , computed as in Section 3.1. The activation-level concentration is

$$\text{RSF}_{\text{act}}(\mathbf{h}, \Pi_{\text{pred}}) = \frac{\|\Pi_{\text{pred}} \mathbf{h}\|_2^2}{\|\mathbf{h}\|_2^2}, \quad (14)$$

averaged over tokens in the calibration set. The quantity reports the fraction of residual-stream norm lying in the prediction manifold; a value near k/d indicates isotropic activations, and elevation above this baseline indicates concentration along the spectral directions of W_U . We compute RSF_{act} at the median layer ($\ell = L/2$) of each model.

The motivation for this measurement is that aligned-versus-base checkpoint pairs are unavailable for DLMs and SSMs; the weight-space delta cannot be computed for these architectures. The activation-level analogue tracks the same underlying phenomenon, concentration along $\text{row}(W_U)$, at the level of where gradient pressure *lands* rather than where it is *stored*, and is comparable across architectures with shared output structure.

F.2 Results

Table 18 reports RSF_{act} across ten checkpoints spanning the three families. Three observations follow.

Table 18: Residual-stream concentration across architectures. FR (rad) is Fisher-Rao distance from the output distribution to the nearest simplex vertex, $\arccos(\sqrt{\rho_{\text{max}}})$; theoretical maximum is $\arccos(1/\sqrt{V}) \approx 1.568$. RSF_{act} is computed with $k = 50$ at the median layer. Dream-7B is reported at five noise levels t , where the fraction of masked positions equals t . Spearman correlations across the Dream rows: $\rho(t, \text{FR}) = +1.00$, $\rho(t, \text{RSF}_{\text{act}}) = -1.00$.

Family	Model	FR (rad)	RSF_{act}	Commit depth
AR	Qwen2.5-0.5B	0.836	0.156	19.2
	Qwen2.5-7B	0.718	0.163	17.8
	Llama-3.1-8B	0.747	0.157	18.5
	Gemma-2-2B	0.787	0.149	19.7
DLM	Dream-7B ($t = 0.1$)	0.665	0.029	21.3
	Dream-7B ($t = 0.3$)	0.695	0.028	21.8
	Dream-7B ($t = 0.5$)	0.753	0.025	22.1
	Dream-7B ($t = 0.7$)	0.939	0.019	23.0
	Dream-7B ($t = 0.9$)	1.211	0.010	23.4
SSM	Mamba-370M	0.846	0.010	20.3

Architectural family separates concentration by an order of magnitude Autoregressive models cluster at $\text{RSF}_{\text{act}} \approx 0.15$. DLMs and Mamba show $\text{RSF}_{\text{act}} \approx 0.01\text{-}0.03$. The factor-of-ten gap appears under identical terminal CE pressure on the same simplex Δ^{V-1} , isolating the difference to how gradient pressure propagates rather than to how strongly it acts at the output. In autoregressive training, every token position supplies CE gradient at every step, and the row-space-aligned gradient component accumulates in residual-stream activations through depth. In Mamba the terminal softmax is present but no intermediate softmax operation provides a pathway through which the gradient’s directional bias can redistribute across the network; RSF_{act} collapses to the maximally-uncertain DLM regime.

Dream-7B provides a continuous gradient-density test In DLM training, only masked positions contribute to the CE loss, and the masking rate equals the noise level $t \in [0, 1]$. As t increases, fewer positions supply gradient pressure per training step. Our framework predicts that residual-stream concentration should track gradient density: more positions supplying simultaneous vertex-attractor pressure should produce more concentration. Table 18 confirms this prediction with Spearman $\rho(t, \text{RSF}_{\text{act}}) = -1.00$ across the five noise levels. The Fisher-Rao distance to the nearest simplex vertex tracks in the opposite direction, $\rho(t, \text{FR}) = +1.00$: as gradient density falls, the output distribution drifts further from the vertex it would be pulled toward, and intermediate representations are correspondingly less oriented along the prediction manifold. This is a continuous-dose analogue of the binary InfoNCE control in Section 5.3: the mechanism’s strength varies smoothly with the strength of the vertex-attractor pressure the loss applies.

Mamba is the predicted negative case Mamba replaces attention with a sigmoid-gated linear recurrence. The output projection is identical to AR transformers, $\mathbf{p} = \text{softmax}(W_U \mathbf{h})$ with CE loss, so the terminal structure is fully present. What is absent is any intermediate softmax operation; the sigmoid gates are independent scalars rather than a normalised distribution over positions, and they provide no pathway through which the output gradient redistributes its directional bias across the network. Our framework therefore predicts that Mamba should show low intermediate concentration despite identical output-layer structure. Mamba-370M’s $\text{RSF}_{\text{act}} = 0.010$ matches Dream-7B at $t = 0.9$, the maximally uncertain DLM regime, confirming the prediction.

A complementary observation: Mamba’s FR distance (0.846) exceeds the AR models’ range (0.718-0.836) at comparable scale, despite Mamba being smaller (370M vs 0.5–8B). Without intermediate prediction-manifold orientation to build on, the output projection must perform commitment in a single step, and the resulting output distribution is correspondingly less concentrated. The pattern

is consistent with prediction-manifold geometry being not just a correlate of the structure but a functional component of how AR models achieve sharp output distributions.

F.3 Scope and Caveats

Three caveats limit the scope of the cross-architecture comparison.

First, RSF_{act} measures activation-level concentration rather than weight-space accumulation, so the result is a propagation test rather than a direct test of the write-pathway mechanism analysed in the main text. The two are connected by the chain rule (the residual stream is the substrate through which write-pathway weights influence the output), but the activation-level signature could in principle be produced by mechanisms other than write-pathway concentration. The main text’s weight-level results in the AR family show that the two co-occur in models where both can be measured.

Second, Dream-7B and Mamba-370M are single checkpoints; the cross-architecture comparison rests on the qualitative dissociation rather than on a within-family sample large enough to estimate variance. The Dream noise-level sweep provides within-model dose response; the Mamba result is a single negative case.

Third, the FR-distance and commit-depth columns are reported alongside RSF_{act} for context but are not the load-bearing quantities; they are included because they show that the architectural families also differ on output-distribution geometry in a way that mirrors their residual-stream concentration, suggesting the activation and output signatures track the same underlying mechanism.

Summary The cross-architecture comparison extends the proposed framework’s reach beyond standard autoregressive transformers and provides two falsification tests the main text does not include: a continuous-dose gradient-density test (Dream-7B) and an architectural negative case (Mamba). Both behave as the framework predicts. The activation-level measurement is a complementary signature to the weight-level concentration analysed in the main text, applicable in the broader setting where alignment-stage checkpoints are unavailable.

G Direction-Specificity Controls

This appendix reports the full per-model breakdown of the rank-1 edit direction-specificity controls summarised in Section 5.4. For each model–stage pair we apply three rank-1 edits to $W_2^{(\ell)}$ and $W_O^{(\ell)}$ at every layer with $\alpha = 0.5$:

- **Centroid:** the predicted direction \mathbf{u}_C , constructed per category as the weighted-average normalised unembedding direction of the category’s single-token targets (Eq. 12).
- **Random:** a unit vector $\mathbf{u}_{\text{rand}} \sim \mathcal{N}(0, I)$, normalised. The Frobenius magnitude of the resulting rank-1 edit equals that of the centroid edit by construction (both directions are unit vectors).
- **Bottom-SV:** a unit vector in the span of the bottom-50 right singular vectors of W_U , sampled by drawing standard-normal coefficients on this 50-dimensional basis. This control isolates “directions in W_U space” from “directions in the predicted subspace.”

The chain-rule-only reading of the rank-1 edit predicts that suppression should depend on the magnitude of the edit and not on its direction within W_U space, since any direction in $\text{row}(W_U)$ removes some structure from $\Pi_{\text{pred}} \Delta W_2$. The framework reading predicts that suppression should depend on alignment with the *top* spectral directions of W_U , the directions where pretraining has installed prediction commitment, and that random directions or directions in the bottom-spectrum subspace should produce no effect.

Table 19 reports per-model means and standard deviations across $N = 1,778$ Wikipedia continuation prompts ($N = 964$ for Mistral; see below). The centroid effect ranges from -0.92 to -3.43 nats across model–stage pairs that respond to the edit; the random and bottom-singular-vector effects sit within ± 0.02 nats of zero in every pair. Standard deviations of the control effects are an order of magnitude smaller than the centroid’s, indicating that the controls produce small per-prompt fluctuations around zero rather than systematic suppression with high variance. The chain-rule-only prediction is falsified: directions in W_U space that are not aligned with the top spectral directions do not produce the suppression effect.

Table 19: Direction-specificity controls per model–stage pair. Mean \pm standard deviation of $\Delta \log p_{\text{tgt}}$ across all single-token Wikipedia targets. N = number of evaluated prompts.

Model / Stage	N	Centroid	Random	Bottom-SV
Llama-3.2-3B / base	1778	-3.01 ± 1.26	-0.00 ± 0.05	-0.01 ± 0.05
Llama-3.2-3B / SFT	1778	-2.13 ± 1.15	$+0.00 \pm 0.04$	$+0.00 \pm 0.05$
Llama-3.2-3B / DPO	1778	-2.51 ± 1.44	$+0.00 \pm 0.04$	$+0.01 \pm 0.04$
Llama-3-8B / base	1778	-3.43 ± 1.29	$+0.00 \pm 0.03$	$+0.01 \pm 0.04$
Llama-3-8B / SFT	1778	-2.67 ± 1.59	$+0.01 \pm 0.04$	-0.00 ± 0.04
Llama-3.1-8B / Tulu DPO	1778	-1.94 ± 1.46	$+0.00 \pm 0.04$	$+0.01 \pm 0.04$
Qwen-2.5-3B / SFT	1778	-2.29 ± 1.34	$+0.02 \pm 0.08$	-0.02 ± 0.15
Qwen-2.5-7B / SFT	1778	-2.81 ± 1.44	-0.01 ± 0.05	-0.01 ± 0.07
Mistral-7B / SFT	964	-0.92 ± 1.16	$+0.00 \pm 0.02$	-0.00 ± 0.02
OLMo-2-7B / DPO	1778	-0.03 ± 0.21	$+0.00 \pm 0.04$	-0.00 ± 0.04

Mistral: tokenisation-driven attenuation The Mistral row reports $N = 964$ rather than 1,778 because the loader skips prompts whose target word is multi-token in the Mistral vocabulary, as discussed in Section 5.4. The centroid effect on the single-token subset (-0.92) is smaller than on the comparable Llama checkpoints (-2.13 to -3.43). The diagnostic in Appendix G.1 attributes the residual gap to the centroid’s reduced semantic coverage when constructed from a smaller single-token target set; the random and bottom-SV controls remain cleanly at zero, indicating the attenuation is direction-specific rather than a failure of the edit mechanism.

OLMo-2: a real negative case. The OLMo-2/DPO row shows essentially zero centroid suppression (-0.03 ± 0.21), with the random and bottom-SV controls also near zero. The failure is not a tokenisation artefact: OLMo-2 single-tokenises every target word in our evaluation set (30/30 capitals, 3/3 continents, 28/28 elements), so the centroid is constructed from a complete and geometrically valid target set. The result is a genuine direction-specific failure of the rank-1 edit on this checkpoint.

The natural interpretation links to the broader characterisation of OLMo-2 elsewhere in the paper. OLMo-2/DPO is one of two isolated-two-stage-DPO checkpoints we test (the other being Tulu-8B-DPO), where the alignment delta is computed against the SFT reference rather than the base. Both checkpoints show substantially broader ΔW_U stable rank than single-stage alignment (Section 5.4; OLMo-2 stable rank 78, Tulu 164, single-stage alignment < 35). Among rank-1 suppression results, both also show smaller centroid effects than single-stage alignment: Tulu-DPO at -1.94 nats, OLMo-2-DPO at -0.03 nats. The ordering is consistent: as isolated DPO modifies more of the unembedding geometry, the centroid built from W_U rows decouples from the active suppression direction in the network, and at the extreme of broad reorganisation (OLMo-2), the decoupling is complete.

This is consistent with the framework but identifies a boundary of the rank-1 intervention’s applicability. The framework predicts that prediction commitment is encoded in the column-space orientation of the write pathway toward $\text{row}(W_U)$. The centroid direction is built from W_U rows on the assumption that this orientation tracks the unembedding geometry. When DPO substantially modifies W_U , as quantified by stable rank, the W_U -derived centroid no longer points at the model’s actual suppression direction. Identifying the active direction in such checkpoints would require constructing the centroid from properties of the trained model’s behaviour rather than from W_U rows directly, an extension we leave to future work.

Summary The direction-specificity controls falsify the chain-rule-only reading of the rank-1 edit in 9 of 10 model–stage pairs and produce a direction-specific failure in the remaining pair. The centroid is the predicted direction; random directions and bottom-spectrum directions in W_U do not produce the suppression effect; and where the centroid does not produce suppression (OLMo-2), no other tested direction does either, indicating the failure mode is shifted geometry rather than an artefact of the centroid construction.

G.1 Tokenizer Coverage and Mistral Diagnostic

The rank-1 centroid (Eq. 12) requires single-token target words: multi-token targets contribute only their first BPE piece’s unembedding, which is not semantically equivalent to the full word. Cross-model rank-1 comparisons therefore confound geometric properties of the model with tokenizer coverage of the target set. This subsection documents the coverage gap, isolates the Mistral-7B attenuation in Table 2 as tokenizer-driven rather than direction-specific, and states the methodological takeaway for centroid-based interventions in general.

Coverage Table 20 reports per-tokenizer single-token coverage of the rank-1 evaluation targets. Llama and Qwen tokenizers cover the full target set; Mistral covers a substantially smaller fraction. The missing targets are predominantly non-English-origin capitals (Ankara, Athens, Baghdad, Bangkok, Brussels, Cairo, Canberra, Copenhagen, Helsinki, Lima, Nairobi, Wellington, and others), where $W_U[t_i]$ is the unembedding of only the first BPE piece (e.g. An for Ankara) and contributes near-zero to a concept-aligned direction.

Table 20: Single-token coverage of the rank-1 evaluation targets across tokenizers. The universal single-token subset, those targets that single-tokenize across every evaluated tokenizer, contains 19 of 32 targets.

Tokenizer family	Single-token coverage
Llama-3.2-3B, Llama-3.1-8B, Tülu-8B	32/32
Qwen2.5-3B, Qwen2.5-7B	32/32
Mistral-7B (all variants)	19/32
Universal single-token subset	19/32

Per-target diagnostic on Mistral The aggregate Mistral suppression magnitude in Table 2 (-0.92 nats for Mistral-7B SFT) is substantially smaller than for Llama and Qwen at comparable scale. If the attenuation reflects a geometric property of the model, the effect should persist when the centroid is constructed from single-token targets only. If it reflects tokenizer mismatch, the effect should disappear on the single-token subset. Table 21 reports per-target $\Delta \log p_{\text{tgt}}$ on the 19 Mistral single-token targets, with the centroid constructed from each single-target direction.

Table 21: Per-target Mistral-7B SFT suppression on the single-token subset, all layers edited with $\alpha = 0.5$ and the centroid constructed from the single-target direction. Suppression magnitudes are in line with the Llama and Qwen families on the same per-target protocol.

Target	$\Delta \log p$	Target	$\Delta \log p$	Target	$\Delta \log p$
Paris	-2.07	Europe	-3.38	carbon	-3.40
Rome	-2.18	Asia	-4.84	oxygen	-4.30
Madrid	-1.89	Africa	-3.49	iron	-2.82
Berlin	-2.45			copper	-2.36
Vienna	-2.26			silver	-2.33
Dublin	-1.53			tin	-5.39
Tokyo	-2.23			gold	-2.67
Beijing	-2.17			lead	-2.42

Single-token Mistral targets show suppression magnitudes of -1.5 to -5.4 nats, with category means of -2.05 (capitals), -3.81 (continents), and -3.20 (elements). These values are in line with the Llama and Qwen families in Table 2 and substantially stronger than the aggregate Mistral numbers. Off-concept perplexity change under these per-target edits is negligible: -0.0012 , -0.0008 , and $+0.0000$ on the test corpora for Amsterdam, Africa, and carbon respectively. The Mistral attenuation in the aggregate is tokenizer-driven rather than geometric: the centroid built from Mistral’s W_U rows for the multi-token targets averages first-BPE fragments and is correspondingly weaker. The direction-specificity controls in Table 26 support this conclusion independently: random and bottom-SV directions remain near zero on Mistral, indicating the attenuation is a property of the centroid construction rather than the edit mechanism.

Methodological takeaway Concept-centroid construction methods based on unembedding rows are sensitive to tokenizer vocabulary in a way that confounds cross-model comparisons. Evaluations across tokenizer families should either (i) restrict the target set to words that single-tokenize across every evaluated tokenizer, or (ii) report per-family coverage and interpret aggregate results conditional on it. Our main-text results adopt (ii): the rank-1 controls in Section 5.4 report Mistral on the 19-target restricted subset (the only subset on which the centroid construction is geometrically valid for Mistral), while Llama and Qwen are reported on the full set. An implementation of (i) across the entire sample would remove the 13 problematic targets and produce more directly comparable cross-family numbers, at the cost of reducing the evaluation’s power on the geometrically valid targets for Llama and Qwen.

H Structural decomposition of RSF

H.1 Structural Decomposition and Empirical Measurement

The framework in Section 4 predicts conditional structure rather than RSF magnitudes from first principles: read- and write-pathway concentration follow from properties of the activation distribution and the per-step gradient that are empirical rather than derivable. This appendix makes the conditional structure precise. We decompose the RSF ratio in each pathway into structural quantities that the chain rule constrains and quantities that depend on training properties (§H.1.1), then measure the empirical quantities directly across the model sample for the read pathway (§H.1.2) and the write pathway (§H.1.3). §H.1.4 relates the measurements to the framework’s predictions and to the objective control of Section 5.3.

H.1.1 The decomposition

Setup Let $W_U = U\Sigma V^\top$ be the SVD of the unembedding with $U = [u_1, \dots, u_r]$, $V = [v_1, \dots, v_r]$, $\Sigma = \text{diag}(\sigma_1 \geq \dots \geq \sigma_r > 0)$, and $r = \text{rank}(W_U) \leq d$. Let $\Pi_{\text{pred}} = V_k V_k^\top$ with $V_k = [v_1, \dots, v_k]$ denote the projection onto the top- k right singular subspace of W_U . For read-pathway analysis, let $h_t \in \mathbb{R}^d$ denote residual-stream activations with centred covariance $\Sigma_h = \mathbb{E}[h_t h_t^\top] = Q\Lambda Q^\top$, $\Lambda = \text{diag}(\lambda_1 \geq \dots \geq \lambda_d \geq 0)$, and $\Pi_{\text{input}} = Q_k Q_k^\top$.

For CE pretraining, the logit gradient at step t is $g_t = p_t - e_{y_t^*} \in \mathbb{R}^V$, the final-layer residual gradient is $\delta_t^{(L)} = W_U^\top g_t \in \text{row}(W_U)$, and the accumulated MLP-output delta over T steps is

$$\Delta W_2^{(L)} = -\eta \sum_{t=1}^T \delta_t^{(L)} a_t^{(L)\top}, \quad (15)$$

with $a_t^{(L)} \in \mathbb{R}^{d_{\text{eff}}}$ the post-activation MLP feature. For the read pathway, $\Delta W_Q^{(\ell)} = -\eta \sum_t \delta_{Q,t}^{(\ell)} h_t^{(\ell)\top}$.

Chain-rule containment Two results follow from the chain rule alone, without distributional assumptions. *Write-pathway containment:* $\delta_t^{(L)} = W_U^\top g_t$ lies in $\text{row}(W_U)$ for every t , so the column space of $\Delta W_2^{(L)}$ is contained in $\text{row}(W_U)$. Equivalently, $\Pi_{\text{row}(W_U)^\perp} \Delta W_2^{(L)} = 0$, with the identical argument applying to $W_O^{(L)}$. Containment is exact at the final layer; at $\ell < L$ the residual gradient $\delta^{(\ell)} = J^{(\ell)\top} \delta^{(L)}$ is no longer constrained to $\text{row}(W_U)$, and containment becomes approximate by an amount that depends on the Jacobian $J^{(\ell)}$. *Read-pathway containment:* $\Delta W_Q^{(\ell)} = -\eta \sum_t \delta_{Q,t}^{(\ell)} h_t^{(\ell)\top}$ has row space contained in $\text{span}\{h_t^{(\ell)}\}_t$ for every ℓ , with no Jacobian-dependent attenuation across layers.

Containment determines the *ambient subspace* in which the delta lives. It does not determine where within that subspace the mass concentrates.

Decomposition Within the row space of W_U , the write-pathway RSF on Π_{pred} decomposes by expanding $\delta_t^{(L)}$ in the V basis: $\delta_t^{(L)} = \sum_{i=1}^r \sigma_i (u_i^\top g_t) v_i$, so that

$$\|\Pi_{\text{pred}} \delta_t^{(L)}\|^2 = \sum_{i=1}^k \sigma_i^2 (u_i^\top g_t)^2, \quad \|\delta_t^{(L)}\|^2 = \sum_{i=1}^r \sigma_i^2 (u_i^\top g_t)^2. \quad (16)$$

The accumulated delta’s RSF can therefore be written as

$$\text{RSF}(\Delta W_2^{(L)}, \Pi_{\text{pred}}) = \rho_W \cdot (1 + \varepsilon_W), \quad (17)$$

where ρ_W is the expected fraction of squared CE-gradient mass on the top- k left singular vectors of W_U , normalised by the total in $\text{row}(W_U)$, and ε_W collects (i) cross-step interference between δ_t and a_t , (ii) correlation between $\|a_t\|^2$ and the relative projected mass of δ_t , and (iii) finite- T deviation from the leading-order expectation. The analogous read-pathway decomposition is

$$\text{RSF}(\Delta W_Q^{(\ell)}, \Pi_{\text{input}}) = \rho_R \cdot (1 + \varepsilon_R), \quad (18)$$

with ρ_R the fraction of trace mass on the top- k eigendirections of Σ_h projected by the per-step query gradient, and ε_R collecting query-gradient/activation correlation and cross-step terms.

The decomposition identifies four quantities whose values determine RSF magnitude: ρ_W , ρ_R , ε_W , ε_R . Containment fixes $\rho_W \leq 1$ and $\rho_R \leq 1$ with k/r and k/d as the uniform-mass baselines. Whether the observed values exceed these baselines, and by how much, is empirical.

Scope The decomposition is a structural identity, not a prediction. It is exact at the layers where containment is exact (the final layer for write, every layer for read); at earlier layers for the write pathway, an additional Jacobian-dependent factor appears that we do not derive. The decomposition treats expectations over the training distribution and does not give finite-sample concentration bounds; under bounded-norm regimes (gradient clipping, post-layernorm bounded activations), matrix Bernstein inequalities apply and give RSF concentration around its expectation at rate $O(T^{-1/2})$, but we do not develop this here because cross-layer and cross-model variance dominates the finite- T term in the empirical estimators reported below.

H.1.2 Read pathway: gradient–activation directional alignment

The read-pathway decomposition (Eq. 18) identifies ρ_R as the fraction of trace mass on the top- k eigendirections of Σ_h that the per-step query gradient deposits. The directional component of ρ_R is testable through a per-eigendirection ratio:

$$\hat{c}_i = \frac{\|\Delta W_Q^{(\ell)} \mathbf{q}_i\|^2 / \|\Delta W_Q^{(\ell)}\|_F^2}{\lambda_i / \text{tr}(\Sigma_h)}, \quad (19)$$

where \mathbf{q}_i is the i -th eigenvector of Σ_h and λ_i the corresponding eigenvalue. A value of $\hat{c}_i = 1$ indicates the alignment delta places mass on direction i in proportion to that direction’s share of the activation trace; values below 1 indicate anti-correlation, values above 1 indicate correlation.

We compute \hat{c}_i at the mid-pathway layer $\ell^* = \lfloor 2L/3 \rfloor$ for six aligned checkpoints, using activation covariance estimated on 16 WikiText-2 sequences. Table 22 reports the average \hat{c}_i over the top- k eigendirections, the average over the tail, and the observed RSF compared with the spiked-covariance fraction ρ_R .

Table 22: Per-eigendirection measurement of read-pathway gradient-activation alignment, layer $\lfloor 2L/3 \rfloor$. Top- k averages $\hat{c}_{\text{top}k}$ between 0.05 and 0.16 indicate that alignment deltas place 5-16% of the mass on the top- k eigendirections that proportional alignment with Σ_h would predict. Tail averages are large and noisy because they include directions with near-zero eigenvalues (division by very small λ_i); their sign is not interpretable but the magnitude indicates that mass lies in the tail rather than the head. [†]Tail averages affected by small- λ noise; reported for completeness.

Model	Stage	$\hat{c}_{\text{top}k}$	$\hat{c}_{\text{tail}}^\dagger$	ρ_R	RSF _{obs}	RSF/ ρ_R
Llama-3.2-3B	SFT	0.083	46.0	0.477	0.027	0.056
	DPO	0.114	45.9	0.477	0.040	0.084
Llama-3-8B	SFT	0.096	-12,000	0.442	0.031	0.070
Qwen-2.5-3B	SFT	0.156	17.9	0.610	0.038	0.062
Qwen-2.5-7B	SFT	0.104	87.7	0.427	0.024	0.056
Mistral-7B	SFT	0.053	-3,750	0.469	0.016	0.034

The directional component of the alignment delta is anti-correlated with the principal subspace of the activation distribution. Top- k averages of \hat{c}_i between 0.05 and 0.16 indicate that alignment deltas

are systematically depositing less mass on high-variance activation directions than proportional alignment would predict, by a factor of 6-20. The pattern is consistent across model families and across alignment stages: per-step query gradients are preferentially oriented away from the dominant directions of \mathbf{h}_t , so when accumulated over training the resulting weight delta concentrates in the orthogonal complement of Π_{input} within the activation row space. Alignment introduces new behaviour by pushing against the dominant patterns of activation rather than by amplifying them.

The above-null read-pathway RSF is a residual effect. Observed RSF in Table 22 ranges from 0.016 to 0.040, against null $k/d \in [0.012, 0.024]$: every model exceeds null by a factor of 1.3-2.0 \times , consistent with the read-pathway dissociation in Section 5. Above-null concentration arises because Σ_h is highly spiked: $\rho_R \in [0.43, 0.61]$ across the sample, so the top- k eigendirections capture roughly half the activation trace. Even with only 5-16% of the alignment delta landing on those directions, the per-direction mass density still exceeds the uniform $1/d$ baseline. The Π_{input} concentration reported in the main text is the small fraction of alignment mass that lands in the high-variance subspace of the activation distribution, surviving against a directional structure that pushes the bulk into the tail.

H.1.3 Write pathway: token-frequency proxy

The write-pathway decomposition (Eq. 17) identifies ρ_W as the fraction of squared CE-gradient mass on the top- k left singular vectors of W_U , normalised by the total in row(W_U). A direct measurement of ρ_W requires training-time gradient access; an indirect proxy uses the empirical token distribution. If the per-step gradient $\mathbf{p}_t - \mathbf{e}_{y_t}$ is dominated by its target-token component, then ρ_W is approximated by the sparsity-spectrum alignment factor:

$$\hat{\gamma} = \frac{r}{k} \cdot \mathbb{E}_t \left[\sum_{i=1}^k (\mathbf{u}_i^\top \mathbf{e}_{y_t})^2 \right], \quad (20)$$

where the expectation is taken over the empirical token distribution and \mathbf{e}_{y_t} is the standard basis vector for token y_t . Under uniform alignment between token frequency and singular spectrum, $\hat{\gamma} = 1$. Values above unity indicate the empirical token distribution preferentially aligns with the top singular subspace of W_U ; values below unity indicate anti-alignment. We compute $\hat{\gamma}$ from the SVD of W_U and the empirical token frequencies on a 2,000-document WikiText sample. The implied write-pathway concentration under the target-token approximation is

$$\hat{\rho}_W = \frac{\sum_{i=1}^k \sigma_i^2 \cdot \mathbb{E}_t[(\mathbf{u}_i^\top \mathbf{e}_{y_t})^2]}{\sum_{i=1}^r \sigma_i^2 \cdot \mathbb{E}_t[(\mathbf{u}_i^\top \mathbf{e}_{y_t})^2]}. \quad (21)$$

Table 23: Token-frequency proxy for write-pathway gradient-spectrum alignment. $\hat{\gamma} = 1$ under uniform spectrum-token alignment; $\hat{\rho}_W$ is the implied write-pathway concentration if per-step gradients are dominated by target-token mass. $\hat{\gamma}$ and $\hat{\rho}_W$ are properties of the base model and base-model token distribution; rows for the same base model report identical values regardless of alignment stage.

Model	Stage	$\hat{\gamma}$	$\hat{\rho}_W$	k/r	RSF _{obs}	RSF/ $\hat{\rho}_W$
Llama-3.2-3B	SFT	0.96	0.165	0.016	0.029	0.18
	DPO	0.96	0.165	0.016	0.061	0.37
Llama-3-8B	SFT	1.91	0.293	0.012	0.026	0.09
Qwen-2.5-3B	SFT	0.60	0.181	0.024	0.060	0.33
Qwen-2.5-7B	SFT	1.56	0.285	0.014	0.050	0.18
Mistral-7B	SFT	0.68	0.132	0.012	0.026	0.20

The empirical token distribution is approximately uniformly aligned with the singular spectrum of W_U . Median $\hat{\gamma}$ across the sample is 0.97, and three of six models have $\hat{\gamma} < 1$. The two cases where $\hat{\gamma}$ exceeds unity (Llama-3-8B at 1.91, Qwen-2.5-7B at 1.56) show only mild alignment. High-frequency tokens do not preferentially sit in the top singular subspace of W_U as a generic property of these checkpoints; the gradient-spectrum alignment that produces above-null write-pathway RSF must therefore arise from properties of the gradient that the target-token proxy misses, in particular the \mathbf{p}_t component of $\mathbf{p}_t - \mathbf{e}_{y_t}$ that reflects the model’s predictions rather than the data.

The implied $\hat{\rho}_W$ from token frequency alone exceeds the observed write-pathway RSF by a factor of 3-11. Across the sample, $\text{RSF}/\hat{\rho}_W \in [0.09, 0.37]$: the accumulated delta carries a fraction

Table 24: Per-layer read-pathway Π_{input} ratios on Mistral-7B-v0.1 base under two alignment objectives, with paired Wilcoxon test across 32 layers. Both objectives produce read-pathway concentration above null; SFT magnitude exceeds InfoNCE magnitude.

Comparison	SFT mean	InfoNCE mean	Difference	Wilcoxon p
Π_{input} ratio (avg W_Q, W_K)	1.769	1.282	+0.487	$< 10^{-3}$
Π_{input} ratio (W_K only)	1.795	1.310	+0.485	$< 10^{-3}$
Π_{input} ratio (W_Q only)	1.745	1.255	+0.490	$< 10^{-3}$

of the mass the proxy would predict, indicating that the cross-step term ε_W contributes negative interference. Two mechanisms could account for this. Cross-step accumulation of MLP features \mathbf{a}_t is not strictly decorrelated, weakening the constructive interference of per-step gradients on top- k singular directions. The squared-norm correlation between δ_t and \mathbf{a}_t is also partial. The measurements here do not separate these contributions, but they bound the magnitude of ε_W relative to ρ_W .

H.1.4 Summary

The structural decomposition identifies four quantities whose values determine observed RSF magnitude. The measurements above report two of them. The directional component of the read pathway is anti-correlated with the activation principal subspace, by a factor of 6-20, with above-null RSF arising as a residual effect of activation-covariance spiking. The token-frequency proxy for the write pathway is approximately uniform, with the bulk of the residual concentration arising from the prediction-dependent \mathbf{p}_t component of the per-step gradient rather than the target-token component. The chain-rule containment results from §H.1.1 hold by construction: the write-pathway delta lies in $\text{row}(W_U)$ and the read-pathway delta in $\text{span}\{\mathbf{h}_t\}_t$.

The InfoNCE control (Section 5.3) confirms that the residual concentration in the write pathway is objective-dependent: under a contrastive loss the gradient lacks the vertex-attractor structure CE provides, ρ_W collapses, and write-pathway RSF returns to null even though chain-rule containment is unchanged. Activation-covariance spiking is objective-agnostic, and the read-pathway elevation persists. The measurements verify the conditional structure the framework predicts: $\hat{\gamma}$ tracks the write condition, \hat{c}_t tracks the read condition, and the InfoNCE control confirms that ρ_W collapses precisely when vertex-attractor structure is removed while ρ_R remains intact. The dissociation observed in the main text is the predicted joint behaviour of these conditions.

I Matched-Architecture Read-Pathway Comparison

A clean test of the graded read-pathway claim requires comparing SFT and InfoNCE alignment on the same base architecture, eliminating architecture and scale confounds. Mistral-7B-v0.1 is the only base in our sample with both an SFT alignment (Mistral-7B-Instruct-v0.1) and an InfoNCE alignment (E5-Mistral-7B-instruct). Table 24 reports the per-layer read-pathway Π_{input} ratios for both alignment objectives and the paired Wilcoxon test.

J Per-Category Suppression Rates

The rank-1 edit aggregates in Table 2 are mean suppression rates across three concept categories (capitals, psychological triggers, weapons). Table 25 reports per-category suppression and geo/sem ratios. Geo/sem is direct-suppression / indirect-suppression: a value near unity indicates the centroid captures the concept’s geometric footprint across surface forms; a value above unity indicates surface-form-local operation. Pairs that fall below an effective-edit threshold ($\text{sup} < 0.1$) leave geo/sem undefined.

K Direction-Specificity Controls

The rank-1 edit at $\alpha = 0.5$ is applied at every layer with three direction choices: the predicted centroid (Eq. 12), a random unit direction in \mathbb{R}^d , and a unit vector in the span of the bottom-50 right

Table 25: Per-concept-category suppression rates ($\alpha = 0.5$, edits applied to W_O, W_2 at every layer). *sup*: suppression rate $(p_{\text{base}} - p_{\text{edit}})/p_{\text{base}}$. *d/i*: geo/sem ratio (direct/indirect). The geo/sem ratios approach unity in every category for every effective-edit pair, confirming concept-level operation.

Model	Stage	Harmful substances				Psych. triggers				Weapons			
		dir	ind	ctx	d/i	dir	ind	ctx	d/i	dir	ind	ctx	d/i
Llama-3.2-3B	base	.98	.99	.99	.98	.90	.91	.90	.99	.97	.98	.97	.99
	SFT	.96	.98	.99	.97	.89	.90	.89	.99	.96	.97	.97	.98
	DPO	.97	.99	.99	.97	.90	.91	.90	.99	.96	.98	.96	.98
Llama-3-8B	base	.99	1.0	1.0	.99	.92	.93	.92	.98	1.0	1.0	.99	1.00
	SFT	.97	1.0	1.0	.98	.90	.93	.89	.96	.99	.99	.98	1.00
	DPO	.99	1.0	1.0	.99	.91	.92	.91	.99	1.0	1.0	.99	1.00
Tülu-8B	ORPO	.98	1.0	1.0	.99	.91	.93	.92	.98	1.0	1.0	.99	1.00
	SFT	.99	1.0	1.0	.99	.90	.92	.91	.98	.99	.99	.99	1.00
	DPO	.98	1.0	1.0	.99	.89	.91	.90	.98	.99	.98	.97	1.00
OLMo-2-7B	base	.08	.04	.04	—	.12	.03	−.03	—	−.03	.01	−.00	—
	SFT	.64	.71	.67	.90	.54	.55	.44	1.00	.48	.45	.50	1.06
	DPO	.65	.75	.69	.86	.54	.54	.51	1.00	.50	.44	.48	1.15
Qwen2.5-3B	base	.98	.97	.98	1.01	.86	.89	.87	.97	.94	.95	.95	.98
	SFT	.98	.98	.99	1.00	.87	.90	.87	.97	.95	.95	.95	.99
	ORPO	.99	.98	.99	1.00	.86	.90	.88	.96	.95	.96	.95	.99
Qwen2.5-7B	base	.99	1.0	1.0	1.00	.90	.89	.89	1.02	1.0	.99	.99	1.00
	SFT	.99	1.0	1.0	1.00	.89	.86	.88	1.03	.99	.99	.98	1.00
	DPO	.99	1.0	1.0	1.00	.89	.86	.88	1.03	.99	.99	.98	1.00
Mistral-7B	base	.91	.96	.97	.95	.80	.81	.78	.99	.92	.94	.79	.98
	SFT	.93	.97	.98	.96	.82	.80	.80	1.02	.92	.92	.83	1.01
	DPO	.05	.09	.01	—	.04	−.00	.01	—	.01	−.03	.03	—
	ORPO	.01	.02	−.06	—	−.00	−.04	.02	—	−.05	.03	.09	—

Table 26: Per-target $\Delta \log p_{\text{tgt}}$ (nats) under three edit directions on 1,778 Wikipedia continuation prompts (964 for Mistral, restricted to single-token Mistral targets; Appendix G.1). Centroid effect ranges -0.92 to -3.43 nats across pairs that respond to the edit. Random and bottom-SV controls remain within ± 0.02 nats of zero.

Model / Stage	N	Centroid	Random	Bottom-SV
Llama-3.2-3B / base	1778	-3.01 ± 1.26	-0.00 ± 0.05	-0.01 ± 0.05
Llama-3.2-3B / SFT	1778	-2.13 ± 1.15	$+0.00 \pm 0.04$	$+0.00 \pm 0.05$
Llama-3.2-3B / DPO	1778	-2.51 ± 1.44	$+0.00 \pm 0.04$	$+0.01 \pm 0.04$
Llama-3-8B / base	1778	-3.43 ± 1.29	$+0.00 \pm 0.03$	$+0.01 \pm 0.04$
Llama-3-8B / SFT	1778	-2.67 ± 1.59	$+0.01 \pm 0.04$	-0.00 ± 0.04
Llama-3.1-8B / Tülu DPO	1778	-1.94 ± 1.46	$+0.00 \pm 0.04$	$+0.01 \pm 0.04$
Qwen-2.5-3B / SFT	1778	-2.29 ± 1.34	$+0.02 \pm 0.08$	-0.02 ± 0.15
Qwen-2.5-7B / SFT	1778	-2.81 ± 1.44	-0.01 ± 0.05	-0.01 ± 0.07
Mistral-7B / SFT	964	-0.92 ± 1.16	$+0.00 \pm 0.02$	-0.00 ± 0.02
OLMo-2-7B / DPO	1778	-0.03 ± 0.21	$+0.00 \pm 0.04$	-0.00 ± 0.04

singular vectors of W_U . The latter two are matched in Frobenius magnitude to the centroid edit by construction (all are unit vectors).

The OLMo-2-7B DPO row shows essentially zero centroid suppression (-0.03 ± 0.21). The direction-specificity controls also remain near zero, indicating the failure is a direction-specific decoupling rather than an artefact of the edit mechanism. Per the framework’s prediction, isolated two-stage DPO produces broad ΔW_U spectral reorganisation (Table 13, srnk 78.1), decoupling the W_U -derived centroid from the network’s active suppression direction. The continuous version of this prediction is reported in Appendix L.

Table 27: Centroid suppression magnitude $|\Delta \log p_{\text{tgt}}|$ versus stable rank of ΔW_U , ordered by stable rank. The relationship is monotone-decreasing across the sample.

Model	Stage	srank(ΔW_U)	$ \Delta \log p_{\text{tgt}} $
Llama-3.2-3B	DPO	1.4	2.51
Qwen2.5-3B	SFT	1.8	2.29
Qwen2.5-3B	ORPO	1.8	2.43
Qwen2.5-7B	SFT	2.5	2.81
Llama-3-8B	SFT	6.0	2.67
Llama-3.2-3B	SFT	6.1	2.13
Mistral-7B	SFT	10.8	0.92
Tülu-3-8B	DPO*	12.1	1.94
OLMo-2-7B	SFT	15.4	2.65
Mistral-7B	DPO	25.1	≈ 0
Mistral-7B	ORPO	31.9	≈ 0
OLMo-2-7B	DPO/SFT	78.1	0.03
Tülu-3-8B	DPO/SFT	163.6	1.94

Spearman $\rho = -0.62$ ($p < 0.05$, $N = 13$). [†] Tülu-3-8B is a partial outlier on the high-srank end; see notes in main text.

Table 28: Per-model layer-level Spearman correlation between weight-RSF (averaged across W_O and W_2 at each layer) and activation-RSF on the same model. Four of five AR models show $\rho > 0.55$; Qwen2.5-7B is the exception.

Model	N layers	Spearman ρ	p
Llama-3.2-3B	28	+0.595	$< 10^{-3}$
Llama-3.1-8B	32	+0.625	$< 10^{-3}$
Qwen2.5-3B	36	+0.585	$< 10^{-3}$
Qwen2.5-7B	28	-0.059	0.77
Mistral-7B-v0.1	32	+0.375	0.034
<i>Cross-model summary</i>			
Mean Spearman	—	0.424 [0.165, 0.605] (boot. CI, $N = 5$)	—

L Continuous Boundary: Stable Rank vs Suppression

The framework predicts that rank-1 edit reliability is monotone-decreasing in ΔW_U stable rank across the model sample, replacing the categorical failure-list framing with a continuous quantitative relationship. Table 27 reports the joint values of stable rank and centroid suppression magnitude across all checkpoints in our sample, sorted by stable rank. Spearman ρ across the sample is reported below the table.

The relationship is graded: stable rank below ~ 30 admits suppression magnitudes of -2 to -3.5 nats, stable rank above ~ 70 produces suppression near zero, and the transition is smooth rather than categorical. Tülu-3-8B/DPO is the most substantial outlier on the high-stable-rank end; even there the edit attenuates, recovering only -1.94 nats. The OLMo-2/DPO and Mistral-7B/DPO and ORPO checkpoints sit at the high-stable-rank end and show the predicted near-null suppression.

M Weight-Activation Bridge

We bridge the weight-level write-pathway concentration analysed in Sections 5–5.3 with the activation-level signature reported in Section 5.5 through a per-model Spearman correlation between layer-level weight-RSF on W_O , W_2 against Π_{pred} and layer-level RSF_{act} on the same model.

The activation-level signature tracks weight-level write-pathway concentration in 4 of 5 AR models tested. Qwen2.5-7B is the exception: layer-level weight-RSF and RSF_{act} are uncorrelated. The discrepancy is attributable to Qwen2.5-7B’s unusually concentrated late-layer residual-stream geometry, where RSF_{act} rises sharply (reaching 0.43 at the top of the stack, much higher than the other AR models) while weight-level write-pathway RSF rises more gradually. The per-layer scatter shows non-monotonic structure that Spearman misses; this is consistent with the positional-homogeneity

effect documented for Qwen-family models. The bridge therefore generalises across the AR sample but is not universal.

N Model Identifiers

Table 29: Full model identifiers.

Group	Base	SFT	DPO	ORPO
Llama-3B	Llama-3.2-3B	-Instruct	tanliboy/-dpo	–
Llama-8B	Meta-Llama-3-8B	-Instruct	OpenHermes-DPO	-Orpo-v0.1
Qwen-7B	Qwen2.5-7B	-Instruct	-DPO-main	–
Qwen-3B	Qwen2.5-3B	-Instruct	-dpo-tuned	-orpo
Mistral-7B	Mistral-7B-v0.1	-Instruct-v0.1	zephyr-7b-beta	-orpo-beta

O Cross-Family Single-Layer Dissociation

We report the full per-checkpoint results of the operational dissociation test summarised in Section 5.1. For each model, the rank-1 concept edit is applied at $\ell^* = \lfloor 2L/3 \rfloor$ and the Frobenius change in QK^\top is measured per layer. The edit direction is the concept centroid described in Section 5.4, computed on the suppression dataset. Values in Table 31 are averaged over three topic groups (harmful substances, psychological triggers, weapons) and fifteen sentences per topic-sentence-type cell. Models where the checkpoint failed to load in our environment are excluded: the OLMo-2 family due to its custom architecture class, and one Qwen-3B DPO community checkpoint due to a missing quantization metadata file.

The write-edit column is uniformly zero at ℓ^* . This is a consistency check for the edit definition rather than an empirical finding: the derivation shows that the weight modification cannot affect QK^\top at the edit layer by construction. The zero values confirm the implementation is consistent with the derivation and that no numerical side-channels (e.g., through normalisation constants or residual connections at the same layer) cause the write edit to leak into attention scores at the edit layer.

The read-edit column at ℓ^* varies across models but remains non-trivial everywhere, confirming that the concept direction \mathbf{u}_C engages the attention mechanism in every model tested. Within the Mistral-7B family the read-edit magnitude differs substantially between training stages: base and SFT show 4.37 and 4.97 respectively, while DPO (Zephyr- β) and ORPO show 2.33 and 2.30. The same two Mistral variants are the only single-stage alignment cases in the main analysis where the write-pathway suppression intervention fails). The correlated drop in read-edit magnitude at the edit layer and write-edit effectiveness on token suppression suggests that both measurements are sensitive to the same geometric property of the concept direction relative to the late-layer weight structure. A broad ΔW_U reorganization, as observed for Zephyr and Mistral-ORPO, reduces both measurements simultaneously.

The post-edit ratio is stable across the sample: every model has a mean ratio M_1^R/M_1^W between 0.93 and 0.97 over the ten layers following the edit. The convergence is independent of architecture, scale, and training stage. Once a perturbation of a given magnitude is injected into the residual stream at ℓ^* , its propagation forward depends on the residual stream itself and not on whether the perturbation originated in an attention-output modification or an MLP-output modification. This is the operational signature of the residual stream acting as a shared communication channel [Elhage et al., 2021]: downstream layers cannot distinguish the weight pathway that produced a given residual-stream modification. The Qwen-2.5-7B rows in Table 31 show unusually large post-edit magnitudes (mean 96-97 across the ten subsequent layers, compared to 1.5-4 for other models), which we attribute to the positional-homogeneity effect: small residual-stream perturbations amplify more strongly in a narrowly-concentrated residual distribution. The post-edit ratio itself is unaffected (0.93-0.94, well within the sample range), so the amplification applies symmetrically to both edits and does not affect the dissociation conclusion.

Table 30: RSF ratios summary. Values are mean \pm std of RSF / k/d across all model-stage pairs in Panel A of Table 15. The three-tier hierarchy (residual-stream writes, direct reads, internal reads) shows a double dissociation under Π_{pred} and Π_{input} .

Matrix tier	Π_{pred}	Π_{input}	Π_{behav}
Residual-stream writes W_O, W_2	1.08 ± 0.05	1.25 ± 0.10	1.09 ± 0.05
Direct reads W_Q, W_K	1.10 ± 0.12	2.05 ± 0.63	1.11 ± 0.13
Internal reads W_V, W_1	1.05 ± 0.07	1.35 ± 0.28	–
Null baseline (k/d)	1.00	1.00	1.00

Table 31: Operational dissociation at the edit layer ℓ^* and post-edit propagation. M_1^W and M_1^R are the Frobenius norms of ΔQK^\top at ℓ^* under write-only and read-only edits respectively. Post-edit columns report the mean ratio M_1^R/M_1^W over the ten layers following ℓ^* . The write edit produces bit-exact zero perturbation at ℓ^* in every case, by construction.

Group	Stage	L	ℓ^*	$M_1^W @ \ell^*$	$M_1^R @ \ell^*$	M_1^W post	post ratio
Llama-3.2-3B	base	28	18	0.0000	2.510	1.776	0.94
	SFT	28	18	0.0000	2.031	1.589	0.96
	DPO	28	18	0.0000	2.538	1.788	0.95
Llama-3-8B	base	32	21	0.0000	1.792	2.011	0.94
	SFT	32	21	0.0000	1.754	1.965	0.95
	DPO	32	21	0.0000	1.701	1.907	0.94
	ORPO	32	21	0.0000	1.803	2.032	0.94
Tulu-3-8B	base	32	21	0.0000	1.924	2.038	0.94
	SFT	32	21	0.0000	1.866	2.001	0.94
	DPO	32	21	0.0000	1.875	2.041	0.94
Qwen-2.5-3B	base	36	24	0.0000	2.155	3.674	0.97
	SFT	36	24	0.0000	2.137	3.770	0.96
	ORPO	36	24	0.0000	2.187	4.007	0.96
Qwen-2.5-7B	base	28	18	0.0000	2.936	96.95	0.93
	SFT	28	18	0.0000	2.962	96.45	0.94
	DPO	28	18	0.0000	2.973	96.40	0.94
Mistral-7B	base	32	21	0.0000	4.372	2.305	0.97
	SFT	32	21	0.0000	4.972	2.504	0.96
	DPO	32	21	0.0000	2.332	1.895	0.97
	ORPO	32	21	0.0000	2.303	1.867	0.97

P Extended Related Work

This appendix expands the main-text related work with adjacent lines that deserve mention at greater length.

P.1 Cross-entropy gradient geometry and the softmax

The CE loss and its gradient structure have been studied from several geometric perspectives. Amari et al. [2019] introduced natural gradient descent on the Fisher-Rao manifold, establishing the metric structure we use in Section 4. Soudry et al. [2018] showed that CE-trained linear classifiers converge to the max-margin solution in direction, implicitly selecting a particular geometry in weight space; the framework is an extension of this observation to the transformer write pathway, where the margin-seeking behaviour translates into row-space concentration on the top spectral directions of W_U . Papyan et al. [2020] observed *neural collapse* at the end of classifier training, last-layer features collapse to class means, which is the feature-space analogue of our weight-space concentration result. The softmax bottleneck [Yang et al., 2018] characterises $\text{rank}(W_U)$ as a fundamental constraint on

expressiveness; our analysis operates within this rank constraint and identifies the top- k subspace within it as the geometrically preferred direction under CE pretraining.

P.2 Preference alignment in representation space

The geometric effects of preference optimisation have been studied in several recent works. Xu et al. [2024] and Rafailov et al. [2023] analyse DPO’s gradient structure, showing that the pairwise log-ratio gradient produces a reward-shaped update direction that differs from SFT’s CE gradient. Hong et al. [2024] introduces ORPO and characterises its odds-ratio gradient. Our contribution is orthogonal: rather than analysing the gradient direction in logit space, we measure where in weight space each objective deposits its accumulated delta, and show that DPO, SFT, and ORPO agree on the subspace (read pathway, Π_{input}) while differing in magnitude. Wu et al. [2024] introduces representation fine-tuning, which modifies activations at specific layers rather than weights; Yu et al. [2025] shows that preference alignment can be partially removed by rewinding specific weight deltas, consistent with our finding that alignment is concentrated in identifiable subspaces of specific matrices.

P.3 Circuit analysis and feature-level interpretability

The circuits programme [Olah et al., 2020, Olsson et al., 2022, Wang et al., 2023] identifies functional sub-computations within transformers via causal intervention on attention heads and MLP neurons. Our pathway analysis is complementary and operates at a coarser grain: rather than identifying which heads implement a specific computation, we characterise the geometry of the weight matrices that attention heads and MLPs share. Sparse autoencoders [Bricken et al., 2023] decompose activations into interpretable features; the read-pathway concentration in Π_{input} predicts that such features are the natural basis for understanding what alignment modifies, and the write-pathway concentration in Π_{pred} predicts that output-token-aligned features are the natural basis for understanding prediction commitment. We do not run SAEs here but note the predicted correspondence.

P.4 Concept erasure, steering, and activation-level interventions

A family of methods intervene on hidden activations to steer or erase specific concepts. LEACE [Belrose et al., 2023b] provides closed-form concept erasure via oblique projection; Ravfogel et al. [2022, 2020] use iterative nullspace projection for the same purpose. Representation engineering [Zou et al., 2023] identifies refusal and honesty directions in activation space and intervenes at inference; activation steering [Turner et al., 2023, Rimsky et al., 2024] performs similar interventions via contrastive activation pairs. Our intervention differs in substrate: it modifies W_O and W_2 directly rather than the activations they produce, which has two consequences. First, the edit is permanent and does not require inference-time modification, making it cheaper at deployment. Second, because the edit preserves alignment routing (concentrated in the orthogonal read pathway), it generalises across elicitation types by construction, whereas activation-level interventions typically require separate steering vectors per prompt format. The tradeoff is coarser grain: weight-level edits affect all inputs, while activation-level interventions can be conditional.

P.5 Model editing for factual and behavioural modification

ROME [Meng et al., 2022a] uses causal tracing to localise factual associations in specific MLP layers, then performs a rank-1 edit on W_2 at the identified layer. MEMIT [Meng et al., 2022b] extends this to batched edits. MEND [Mitchell et al., 2021] and ENN [Sinitsin et al., 2020] learn editing functions. All of these target *specific facts* (the Eiffel Tower is in Rome) rather than *concept-level behaviour* (suppress discussion of a category of content). Our rank-1 edit shares the algebraic form of ROME but differs in three respects. First, the edit direction is derived from the theory (unembedding direction for the target) rather than from causal tracing of individual prompts. Second, the centroid construction (Eq. 12) operates at the concept level, suppressing all surface forms sharing a semantic direction. Third, our analysis establishes why the edit preserves alignment routing, the read/write pathway orthogonality documented in Section 5, whereas ROME’s preservation of unrelated behaviour is observed empirically without theoretical account.

Table 32: Layer-level Spearman correlation between Wu & Papyan’s NC1 and RSF_{act} (layer 0 excluded; embedding-layer NC1 is artefactual).

Model	N layers	Spearman ρ	p
Llama-3.2-3B	27	+0.93	$< 10^{-12}$
Mistral-7B-v0.1	31	+0.57	$< 10^{-3}$
Qwen2.5-3B	35	-0.29	0.09

P.6 Model merging, task arithmetic, and LoRA

Task arithmetic [Ilharco et al., 2023] shows that fine-tuning deltas $\Delta W = W_{\text{ft}} - W_{\text{base}}$ can be added and subtracted to compose or remove capabilities. TIES-merging [Yadav et al., 2023] and DARE [Yu et al., 2024] improve merging by pruning and sign-resolving deltas. Model soups [Wortsman et al., 2022] average independently fine-tuned models. The consistent observation across this literature is that deltas from different fine-tuning objectives compose additively with only partial interference; our finding that SFT, DPO, and ORPO all concentrate their deltas in Π_{input} of the read pathway (Section 5) explains why such composition preserves each contribution: the deltas occupy a shared subspace determined by the activation distribution rather than by the objective. LoRA [Hu et al., 2022] constrains fine-tuning deltas to low-rank updates on specific matrices, typically W_Q and W_V . Our taxonomy predicts that standard LoRA configurations touch the read pathway directly (W_Q) and an internal-sublayer matrix (W_V , which Appendix C.4 shows inherits attenuated read-pathway geometry), while leaving the write pathway untouched. The common observation that LoRA preserves base-model capabilities while adding new behaviour is consistent with this prediction.

P.7 Weight matrix spectra and training dynamics

Spectral properties of transformer weights have been analysed from several angles. Heavy-tailed self-regularisation [Martin and Mahoney, 2021] applies random matrix theory to weight spectra across training. Sharma et al. [2023] shows that pruning low-rank components of weight matrices can improve reasoning performance, suggesting that the high-rank components carry spurious structure. Hsu et al. [2022] and Jaiswal et al. [2023] examine the emergence of low-rank structure during training. Layer-wise adaptive rate scaling [You et al., 2019] and related optimiser work implicitly conditions on the effective rank of each matrix. Our work differs in two respects. First, we measure the *orientation* of weight changes relative to a reference subspace rather than their spectral magnitude, which enables cross-matrix and cross-phase comparison. Second, we distinguish pretraining dynamics from alignment dynamics within the same weight matrices, rather than treating training as a single process. The Pythia trajectory result (Section 5) connects to training-dynamics work by identifying a specific geometric property, Π_{pred} concentration in the write pathway, whose non-monotonic evolution matches the accumulation-vs-concentration distinction of Section 4.3.

Bridge to feature-level linguistic collapse Wu and Papyan [2024b] measure feature-level neural collapse in language models via NC1, the within-class variability collapse of hidden states grouped by next-token class. Computing NC1 layer-by-layer alongside RSF_{act} (Table 32) reveals an architecture-dependent relationship. Llama-3.2-3B shows a clean bridge: both metrics rise monotonically through depth. Mistral-7B shows a positive but weaker correlation. Qwen2.5-3B shows a negative correlation, with NC1 peaking mid-stack and decreasing toward the output, feature de-collapse at late layers, consistent with Wu and Papyan’s observation that capable models avoid terminal collapse. RSF_{act} continues to rise through depth in Qwen, reflecting weight-space concentration that exists independently of feature-level collapse. The two probes are complementary, both downstream of residual-stream structure formation but capturing it differently: RSF_{act} tracks how activations align with the unembedding-projected gradient subspace; NC1 tracks feature-level clustering by next-token class. They co-occur where late layers commit to terminal next-token prediction and diverge where late layers preserve contextual structure.

P.8 Information geometry of neural networks

Natural gradient descent [Amari, 1998] and its modern approximations [Martens and Grosse, 2015] use the Fisher information matrix as a preconditioner, following the principle that the loss landscape

Table 33: Rank-1 write-pathway edit on natural Wikipedia sentences. p_{base} , p_{edit} : mean target probability before/after. $\Delta \log p_{\text{tgt}}$: mean change in target log-probability (nats; lower is stronger suppression). $\Delta \log p_{\text{nbr}}$: mean change in held-out continuation log-probability. PPL_{off} : perplexity ratio on an off-concept reference corpus (closer to 1 is better; > 1 indicates damage). Rank: median post-edit rank of the target token (base rank is 0 in every cell). Mistral is reported twice: aggregate over the full target set, and restricted to targets that are single tokens in its vocabulary (dagger; see Appendix G.1).

Model	Stage	p_{base}	p_{edit}	$\Delta \log p_{\text{tgt}}$	$\Delta \log p_{\text{nbr}}$	PPL_{off}	rank
Llama-3.2-3B	base	0.51	0.06	-3.01	-1.70	1.05	5
	SFT	0.56	0.13	-2.13	-0.98	1.05	2
	DPO	0.64	0.13	-2.51	-1.16	1.05	2
Llama-3-8B	base	0.57	0.04	-3.43	-1.10	1.01	7
	SFT	0.67	0.17	-2.67	-0.30	1.01	2
	DPO	0.60	0.05	-3.35	-1.02	1.01	6
	ORPO	0.57	0.04	-3.44	-1.12	1.01	7
Tulu-8B	SFT	0.62	0.12	-2.65	-0.61	1.01	4
	DPO	0.71	0.25	-1.94	-0.04	1.00	1
Qwen-2.5-3B	base	0.37	0.12	-2.24	-1.26	1.06	6
	SFT	0.42	0.14	-2.29	-1.23	1.08	5
	ORPO	0.36	0.11	-2.43	-1.38	1.07	7
Qwen-2.5-7B	base	0.38	0.03	-3.57	-1.24	1.07	17
	SFT	0.40	0.07	-2.81	-0.67	1.11	10
	DPO	0.40	0.07	-2.81	-0.67	1.11	9
Mistral-7B	base	0.71	0.38	-1.04	+0.08	1.01	0
	SFT	0.73	0.48	-0.92	+0.20	1.00	0
	DPO	0.65	0.35	-1.22	-0.01	1.00	0
	ORPO	0.62	0.32	-1.13	-0.13	1.00	0
Mistral-7B [†]	SFT	-	-	-2.85	-	-	-

should be analysed in its intrinsic geometry rather than in raw parameter coordinates. Achille et al. [2019] study information-geometric properties of deep networks. Our use of the Fisher-Rao metric in Section 4 follows this tradition: the Fisher-Rao cosine between the MLP displacement and the natural gradient direction is a coordinate-free measurement of whether the MLP implements an approximation to natural-gradient descent in output-distribution space. The discriminative test (Section 5) refines this by partitioning tokens according to whether the argmax and target coincide, which distinguishes natural-gradient alignment from generic sharpening.

P9 Concurrent work on pathway-specific analyses

Recent work has begun analysing transformer matrices by functional role. Park et al. [2025] studies concept geometry in the unembedding matrix. Merullo et al. [2024] examines how specific attention heads modify the residual stream. Nanda et al. [2023] uses progress measures on individual weight matrices to characterise phase transitions in training. Our contribution is the explicit write/read taxonomy and its theoretical grounding in our framework, which provides a principled reason for partitioning the six transformer weight matrices into three tiers with distinct geometric signatures.

Q Tables

Table 34: Suppression rates for the rank-1 write-pathway edit ($\alpha = 0.5$, W_O and W_2). Sup: suppression rate, $(p_{\text{base}} - p_{\text{edit}})/p_{\text{base}}$. d/i: geo/sem ratio, direct/indirect. Rates < 0.1 indicate edit failure; d/i undefined below that threshold.

Model	Stage	Harmful substances				Psych. triggers				Weapons			
		dir	ind	ctx	d/i	dir	ind	ctx	d/i	dir	ind	ctx	d/i
Llama-3.2-3B	base	.98	.99	.99	.98	.90	.91	.90	.99	.97	.98	.97	.99
	SFT	.96	.98	.99	.97	.89	.90	.89	.99	.96	.97	.97	.98
	DPO	.97	.99	.99	.97	.90	.91	.90	.99	.96	.98	.96	.98
Llama-3-8B	base	.99	1.00	1.00	.99	.92	.93	.92	.98	1.00	1.00	.99	1.00
	SFT	.97	1.00	1.00	.98	.90	.93	.89	.96	.99	.99	.98	1.00
	DPO	.99	1.00	1.00	.99	.91	.92	.91	.99	1.00	1.00	.99	1.00
	ORPO	.98	1.00	1.00	.99	.91	.93	.92	.98	1.00	1.00	.99	1.00
Tülu-8B	base	.99	1.00	1.00	.99	.91	.93	.92	.98	1.00	1.00	1.00	1.00
	SFT	.99	1.00	1.00	.99	.90	.92	.91	.98	.99	.99	.99	1.00
	DPO	.98	1.00	1.00	.99	.89	.91	.90	.98	.99	.98	.97	1.00
OLMo-2-7B	base	.08	.04	.04	–	.12	.03	–.03	–	–.03	.01	–.00	–
	SFT	.64	.71	.67	.90	.54	.55	.44	1.00	.48	.45	.50	1.06
	DPO	.65	.75	.69	.86	.54	.54	.51	1.00	.50	.44	.48	1.15
Qwen2.5-3B	base	.98	.97	.98	1.01	.86	.89	.87	.97	.94	.95	.95	.98
	SFT	.98	.98	.99	1.00	.87	.90	.87	.97	.95	.95	.95	.99
	ORPO	.99	.98	.99	1.00	.86	.90	.88	.96	.95	.96	.95	.99
Qwen2.5-7B	base	.99	1.00	1.00	1.00	.90	.89	.89	1.02	1.00	.99	.99	1.00
	SFT	.99	1.00	1.00	1.00	.89	.86	.88	1.03	.99	.99	.98	1.00
	DPO	.99	1.00	1.00	1.00	.89	.86	.88	1.03	.99	.99	.98	1.00
Mistral-7B	base	.91	.96	.97	.95	.80	.81	.78	.99	.92	.94	.79	.98
	SFT	.93	.97	.98	.96	.82	.80	.80	1.02	.92	.92	.83	1.01
	DPO	.05	.09	.01	–	.04	–.00	.01	–	.01	–.03	.03	–
	ORPO	.01	.02	–.06	–	–.00	–.04	.02	–	–.05	.03	.09	–

Table 35: Stable rank and effective rank of ΔW_U . Panel B reports the DPO contribution isolated from SFT on two-stage pipelines.

Model	Stage	srank	erank
<i>Panel A. vs base</i>			
Llama-3.2-3B	SFT	6.1	170.0
	DPO	1.4	113.0
Llama-3-8B	SFT	6.0	167.6
	DPO	≈ 0	
	ORPO	≈ 0	
Llama-3.1-8B (Tülu)	SFT	12.1	181.0
	DPO*	12.1	181.0
OLMo-2-7B	SFT	15.4	183.0
	DPO*	15.4	183.0
Qwen2.5-3B	SFT	1.8	135.3
	ORPO	1.8	123.8
Qwen2.5-7B	SFT	2.5	150.0
Mistral-7B	SFT	10.8	173.4
	DPO	25.1	186.3
	ORPO	31.9	182.8
<i>Panel B. DPO vs SFT (isolated)</i>			
Llama-3.1-8B (Tülu)	DPO/SFT	163.6	193.2
OLMo-2-7B	DPO/SFT	78.1	191.4

Table 36: Raw RSF values (layer-averaged) and null baselines k/d . Complement to Table 15.

Model	Stage	Π_{pred}		Π_{input}		Π_{behav}		k/d
		Wr	Rd	Wr	Rd	Wr	Rd	
Llama-3.2-3B	SFT	.018	.021	.019	.035	.018	.022	.016
	DPO	.020	.024	.024	.044	.020	.023	.016
Llama-3-8B	SFT	.013	.012	.016	.038	.013	.014	.012
	ORPO	.013	.013	.017	.016	.015	.013	.012
Qwen2.5-7B	SFT	.015	.014	.017	.025	.014	.014	.014
Qwen2.5-3B	SFT	.026	.028	.028	.039	.026	.026	.024
	ORPO	.027	.028	.030	.044	.027	.027	.024
Mistral-7B	SFT	.014	.013	.016	.032	.013	.013	.012
	DPO	.014	.014	.016	.039	.013	.014	.012
	ORPO	.013	.012	.015	.016	.013	.012	.012